Combining Focused Ion Beam Patterning and Atomic Layer Deposition for Nanofabrication

Zhongmei Han

Department of Chemistry

Faculty of Science

University of Helsinki

Finland

ACADEMIC DISSERTATION

To be presented, with the permission of the Faculty of Science of the University of Helsinki, for public examination in Auditorium A110 of the Department of Chemistry (Chemicum), A. I. Virtasen aukio 1, on September 7th 2018, at 12 o'clock noon.

Helsinki 2018

Supervisors

Doctor Marko Vehkamäki
Professor Mikko Ritala
Professor Markku Leskelä
Department of Chemistry
University of Helsinki
Helsinki, Finland

Reviewers

Professor Francesc Pérez-Murano
Instituto de Microelectrónica de Barcelona
Bellaterra, Spain

Assistant Professor Adrie Mackus
Department of Applied Physics
Eindhoven University of Technology
Eindhoven, Netherlands

Opponent

Professor Ilkka Tittonen
Department of Electronics and Nanoengineering
Aalto University
Espoo, Finland

© Zhongmei Han

ISBN 978-951-51-4378-5 (paperback)
ISBN 978-951-51-4379-2 (PDF)
http://ethesis.helsinki.fi/

Unigrafia
Helsinki 2018

千里之行，始于足下。　　　—老子

Abstract

For nanofabrication of silicon based structures, focused ion beam (FIB) milling is a top-down approach mainly used for prototyping sub-micron devices, while atomic layer deposition (ALD) is a bottom-up approach for depositing functional thin films with excellent conformality and a nanometer level accuracy in controlling film thicknesses. Combining the strengths of FIB milling with ALD provides new opportunities for making 3D nanostructures. In FIB milled silicon, the gallium implanted surface suffers from segregation and roughening upon heating, which makes the thermal stability of the as-milled substrate a concern for the following ALD processes which are typically performed at temperatures of 150 °C and higher.

This study aimed to explore methods for improving the thermal stability of FIB milled silicon structures for the following ALD processes. The other aim was to fabricate nanostructures by alternately using FIB milling and ALD approaches on silicon and oxide thin film materials.

The experiments were started on the reduction of gallium implantation during FIB milling of silicon substrates using different incident angles. Oblique incidence of the ion beam was found an effective method for improving the thermal stability of the FIB milled silicon surfaces by decreasing their gallium content. The improved thermal stability allowed to apply ALD Al_2O_3 on the FIB milled surfaces to make nanotrenches. Wet etching in KOH/H_2O_2 was found as a second method for improving the thermal stability by removing the gallium implanted silicon layer. ALD Al_2O_3 thin films can be applied as milling masks to limit amorphization of silicon upon FIB milling. With the aid of KOH/H_2O_2 etching, nanopore arrays, nanotrenches and nanochannels were fabricated. ALD grown $Al_2O_3/Ta_2O_5/Al_2O_3$ multilayers were FIB milled and wet etched to form both 2D and 3D hard masks. The fabricated 2D masks were used for making metal structures which are applicable for electrical connections. Thin film resistors were also fabricated using this 2D mask system.

In conclusion, this study illustrates that combining FIB patterning and ALD is feasible for 3D nanofabrication when the stability of FIB milled surfaces is considered and improved.

Keywords: atomic layer deposition, focused ion beam, nanofabrication, wet etching, gallium removal, hard mask, multilayers, thin film resistors, 3D

Preface

The research and experimental work included in this dissertation were carried out during the years 2011-2018 in the ALD group at the Department of Chemsitry, University of Helsinki.

I would like to express my sincere gratitude to my supervisors. I am really grateful to Professor Mikko Ritala and Professor Markku Leskelä for giving me the opportunity to work in this ALD thin film group from the beginning, for the continuous guidance and support during these years, and for their amazing responsiveness and knowledgeability which will keep influencing me in the future of my life. I am also grateful to my supervisor Doctor Marko Vehkamäki. I could not go this far without him. This research and dissertation were done with kind guidance and attention from all the three supervisors. Their serious scientific attitude, rigorous scholarship and working style deeply inspired me.

I am really grateful to the preliminary examiners of this dissertation, Professor Francesc Pérez-Murano and Assistant Professor Adrie Mackus, for their encouragement and timely review process. Their precious review statements helped improve this dissertation in all aspects. Professor Ilkka Tittonen is thanked for being the opponent of this work.

I would like to gratitude to all the co-authors who contributed to my work. Emma Salmi is thanked for the aid of ALD film growth and Kenichiro Mizohata for elastic recoil diffraction analysis. I am grateful to Miika Mattinen for the time he spent teaching me about AFM. Dr Marianna Kemell and Jani Hämalainen are thanked for helpfulness discussion related to FESEM and ALD reactors, respectively. Also, all the former and present colleagues are thanked for their kindness, helpfulness, and creating of harmonious working atmosphere.

The research leading to this dissertation received financial support from China Scholarship Council (File No. 2011704017), the Finnish Center of Excellence in Atomic Layer Deposition (ALD-CoE) funded by the Academy of Finland, and the doctoral programme in Materials Research and Nanosciences (MATRENA) in the university.

I own my sincere appreciation to my parents, Zengpei (韩增培) and Caihua (何蔡花), and to my younger brother Zhongzhi (韩忠志), for constantly supporting me throughout the years. I also thank my friends for their trust and all the enjoyable moments. Finally, I want to express my gratitude to my husband Ya (赵亚) for understanding and enjoying my challenging life, and to my son Yihan (赵亦涵) and daughter Hanxiao (赵涵晓) for their love during these years.

Helsinki, June 2018

Zhongmei Han

List of publications

This dissertation is based on the following publications which will be referred to in the text by their Roman numberals. The author's contribution to each paper is also described.

I **Combining Focused Ion Beam and Atomic Layer Deposition in Nanostructure Fabrication**
Zhongmei Han, Marko Vehkamäki, Markku Leskelä and Mikko Ritala *Nanotechnology,* 2014, **25**, 115302

The author designed and performed the experiments with help of M.V., did the SEM and EDS analyses, wrote the first draft of the paper and finalized it with the co-authors.

II **Selective Etching of Focused Gallium Ion Beam Implanted Regions from Silicon as a Nanofabrication Method**
Zhongmei Han, Marko Vehkamäki, Miika Mattinen, Emma Salmi, Kenichiro Mizohata, Markku Leskelä and Mikko Ritala *Nanotechnology*, 2015, **26**, 265304

The author designed and performed the FIB experiments with M.V. and ALD with E.S., did the SEM, EDS and AFM analyses (help from M.M for AFM), wrote the first draft of the paper and finalized it with M.V, M.L. and M.R..

III **Resistless Fabrication of Embedded Nanochannels by FIB Patterning, Wet Etching and Atomic Layer Deposition**
Zhongmei Han, Marko Vehkamäki, Markku Leskelä and Mikko Ritala *Proceedings of the 15th IEEE International Conference on Nanotechnology,* 2015, **July 27-30, Italy**, 1008-1011

The author performed the experiments, did the SEM analyses, wrote the first draft of the paper and finalized it with the co-authors.

IV **Metal Oxide Multilayer Hard Mask System for 3D Nanofabrication**
Zhongmei Han, Emma Salmi, Marko Vehkamäki, Markku Leskelä and Mikko Ritala *Nanotechnology*, 2018, **29**, 055301

The author designed and performed all the experiments with help of M.V., did the SEM analyses, wrote the first draft of the paper and finalized it with M.V, M.L. and M.R..

Abbreviations and acronyms

2D	2 dimensional
3D	3 dimensional
AFM	atomic force microscopy
ALD	atomic layer deposition
ASP	anode spot plasma
CVD	chemical vapor deposition
EBL	electron beam lithography
EDS	energy dispersive X ray spectrometry
EHD	electrohydrodynamic
ERDA	elastic recoil detection analysis
eV	electronvolt
FIB	focused ion beam
FIM	field ion microscope
GFIS	gas field ionization source
ICP	inductively coupled plasma
LMIS	liquid metal ion source
NIL	nanoimprinting lithography
PVD	physical vapor deposition
SAMs	self-assembled monolayers
SEM	scanning electron microscope
SERS	surface-enhanced Raman scattering
SIM	scanning ion microscope
SIMS	secondary ion mass spectroscope
SPL	scanning probe lithography
SRIM	stopping and range of ions in matter
STM	scanning tunneling microscope
TEM	transmission electron microscope
TMA	trimethylaluminum
TMAH	tetramethylammonia hydroxide
TOF-ERDA	time-of-flight elastic recoil detection analysis

Table of contents

Abstract 5
Preface 6
List of publications 7
Abbreviations and acronyms 8
Table of contents 9
1 Introduction 11
2 Background 12
2.1 Nanostructure fabrication 12
2.1.1 Nanotechnology and nanofabrication 12
2.1.2 Nanofabrication methods 12
2.2 FIB technology and applications 15
2.2.1 Ion sources for FIB instruments 16
2.2.2 Basic functions and applications of FIB systems 18
2.2.3 FIB-induced damage 21
2.3 ALD in nanotechnology 24
2.3.1 Chemical composition control in ALD 24
2.3.2 Dimensional control in ALD 26
3 Experimental 29
3.1 Structure fabrication 29
3.2 Analysis and characterization 30
4 Results and discussion 31
4.1 Thermal stability of FIB milled silicon surfaces 31
4.1.1 Oblique incident ion beam 32
4.1.2 Wet etching by KOH/H_2O_2 35
4.2 Thermal stability of FIB milled Al_2O_3 and Ta_2O_5 thin films 40
4.3 Nanostructure fabrication 42
4.3.1 Nanopore arrays on silicon 42
4.3.2 Nanotrenches on silicon 44

4.3.3 Ta_2O_5 micro- and nanochannels 46

4.3.4 Ta_2O_5 nanowires 48

4.3.5 2D and 3D hard masks 49

5 Conclusions 56

References 57

1 Introduction

Materials with structures at the nanoscale generally have unique physical, optical, electronic and chemical properties. Shrinking feature sizes have been successfully developed and applied for nanotechnology and nanostructure fabrication to achieve advantages such as lower power consumption, better performance and higher efficiency. Nanostructure fabrication involves creation of functional structures and fine-tuning their dimensions and shapes to get the desired properties.

There are many methods for making nanostructures, divided into top-down and bottom-up approaches, such as photolithography, electron beam lithography (EBL), nanoimprinting lithography (NIL), focused ion beam (FIB) direct-writing, self-assembly, and thin film deposition. FIB direct writing has the capability to make structures without a resist with a sub-10 nanometers resolution. This top-down technique is valuable for nanoscale fabrication especially for prototyping devices, by means of milling and implantation. Atomic layer deposition (ALD) is a thin film growth technique that deposits uniform and conformal films by a self-limiting and layer-by-layer growth mechanism. This mechanism makes ALD a versatile bottom-up technique for nanostructure fabrication with atomic level control of film thicknesses and chemical compositions.

The advantages of these two techniques, FIB and ALD, make motivations of this study to combine the strengths of the top-down of FIB and bottom-up of ALD for nanostructure fabrication. The combination and alternate application of FIB direct-writing and ALD can be exploited to fabricate high-precision 3D nanostructures without any templates or resists. However, the undesired ion implantation and beam damage are issues, both when the ALD process follows on a FIB direct-written surface and when the ALD films are the target for the FIB direct-writing.

The first goal of this dissertation was to study and improve the stability of gallium FIB milled silicon surfaces as the gallium implantation causes segregation and roughens the milled surfaces. The second goal was to study the implantation issue of FIB milling on ALD grown thin films that needs to be addressed on case-by-case basis. The last and final goal was to fabricate nanostructures by combining FIB patterning and ALD.

The structure of this thesis is as follows. Chapter 2 provides a general overview of nanotechnology and nanofabrication, FIB direct-writing and ALD of functional materials with tunable sizes. Chapter 3 describes the experimental details including structure fabrication by FIB and ALD with the aid of chemical etching, and structure characterization. Chapter 4 discusses the experimental results and finally Chapter 5 draws the conclusions.

2 Background

2.1 Nanostructure fabrication

2.1.1 Nanotechnology and nanofabrication

Nano, in Greek, means "dwarf". Nanometer (nm) is a unit of length and one nm is one billionth of a meter (10^{-9} m). Nanotechnology is defined as the manipulation of matter with at least one dimension sized 1-100 nm. In 1959, Richard Feynman stated the possibility of manipulating things atom by atom[1], which seeded the concept of nanotechnology. The term 'nano-technology' was firstly proposed by Taniguchi Norio in 1974[2]. After that, scientists have striven for experimental advances in nanotechnology and there were two major breakthroughs in the 1980s. Gerd Binning and his coworkers, from IBM research laboratory, invented a scanning tunneling microscope (STM)[3] in 1982 and made it capable of both taking images of individual atoms and moving a single atom or molecule. The second breakthrough was the discovery of C_{60} fullerene in 1985 by Harry Kroto et al[4], which led to a work on related carbon nanotubes. A second microscope analogous to STM, atomic force microscope (AFM), was invented by Gerd Binning et al. in 1986[5]. In 1989 STM was for the first time successfully used to manipulate individual atoms into places by Donald Eigler who spelt "IBM" with Xe atoms on a nickel surface[6]. At that point, the eyes and fingers for nanotechnology research had been created.

Nanofabrication is one of the branches of nanotechnology and is also called nanolithography. A fabricated nanostructure has at least one lateral dimension sized 1-100 nm. The desire for nanoscale control of matter has promoted development of a wide variety of nanofabrication methods. There are generally two approaches to make nanostructures, top-down and bottom-up[7]. The top-down approach seeks to scale down larger structures to the nanoscale using microfabrication methods to cut, mill, and shape materials into the desired size and shape. For instance, photolithography, electron beam lithography, nanoimprinting lithography and FIB milling are top-down nanofabrication methods. The bottom-up approach, in contrast, aims to build up nanostructures with small blocks from atoms or molecules, using controlled chemical reactions including self-assembly and thin-film deposition.

2.1.2 Nanofabrication methods

Photolithography

Improvements in the microelectronics industry have been achieved largely by advances in lithography with yield increases, cost reduction and resolution enhancement[8]. Photolithography is widely implemented in manufacturing and known as the conventional

lithography method. Photolithography involves light sources, masks, and photoresists applied on the substrate. The masked irradiation with energetic photons from the light source exposes the photoresist to modify its solubility in the developer. Either the exposed (positive photoresist) or the unexposed (negative photoresist) regions are dissolved during the development of the resist. Subsequent etching step transfers the resist pattern into structures on the substrate surface.

UV light is commonly used as the exposure source for photolithography. The lithography resolution increases as the exposure wavelength decreases. Thus, the resolution can be enhanced by light sources with shorter wavelengths[8, 9] (248 nm KrF, 193 nm ArF, 157 nm F_2, 10-50 nm extreme ultra-violet, and <10 nm soft X-rays) or by applying liquid immersion technology which reduces the effective wavelength[10, 11]. In addition to the wavelength reduction, there are other resolution enhancement technologies in the photolithography systems, such as phase-shift masks, advanced photoresist materials and optical proximity correction[12-14].

Electron beam lithography (EBL)

EBL has a similar working principle to photolithography but the exposure source is an electron beam rather than a light source[15]. Also, no mask is used between the exposure source and the resist because the focused electron beam is small enough for direct writing. The e-beam resist is chemically sensitive to the electron irradiation and can be developed in a specific solvent. The fine structure in the resist can be subsequently transferred to the underlying material by etching or lift off[16]. EBL has the capability of direct writing patterns with an extremely high resolution[17, 18] (less than 5 nm) and large depth of focus[8]. This maskless lithography method can be used to produce photomasks and to fabricate 3D fine structures for semiconductor devices. The disadvantages of EBL are mainly the high cost of the instrument, its maintenance and low throughput compared to photolithography. The low throughput limits its application on large areas. The throughput can be improved by arrays of beams and high-sensitivity resist materials[14, 16].

Scanning probe lithography (SPL)

SPL fabricates nanoscale structures by scanning a small tip on a solid substrate and using mechanical, thermal, chemical and electrostatic interactions to selectively remove, deposit or modify regions of the target surface under the tip[19-21]. Subsequent modification processes, usually chemical, are sometimes needed for the creation of functional structures. Tips from scanning probe microscopy, typically STM and AFM, are used as scanning probes with nanoscale resolution in direct or indirect approaches. For example, thermochemical nanofabrication of graphene oxide has been realized by contacting a heated AFM tip on graphene[22]. Dip-pen has also been applied as a direct-writing and maskless SPL to deliver molecules coated on an AFM tip onto a substrate[23], like transporting ink onto a paper. Multiple probes for parallel nanolithography have been developed for higher

throughput of SPL[19] and probe arrays consisting of multifunctional probe tips for simultaneous patterning and imaging have been used[24].

Nanoimprinting lithography (NIL)

NIL has been developed as a high-throughput, high resolution and low-cost patterning technology. It contains steps such as resist coating on a substrate, compression molding to create a thickness contrast into the softened resist layer, solidifying and demolding, and pattern transfer by etching[25]. NIL is a mechanical process. It overcomes the limits of light diffraction and beam scattering. On the other hand, as NIL imprints a pattern by direct contact between the mold and resist, it often generates defects[26]. There are many variations of NIL for the patterning and pattern transfer process for specific applications. For example, UV-assisted nanoimprint applies a UV curable resist to avoid the heating and thermal expansion mismatch between the mold and the resist[27]. Roll-to roll nanoimprinting has also been developed to fabricate nanostructures with improved throughput on flexible substrates[28].

Focused ion beam direct writing

In FIB processing, ions are accelerated and focused into a fine beam onto a solid surface where they interact with the target atoms. The ion-solid interaction generates secondary electrons and ions for imaging, causes physical sputtering, atom replacement, and even chemical reactions when gas species are present. Therefore, FIB has been widely used in the field of materials characterization and micro/nanofabrication for imaging, milling, ion implantation, and deposition[29]. The ion imaging has a lower resolution, in most cases, compared with SEM and causes damage to the surface of interest. A SEM-combined FIB system, usually called a dual beam system, can avoid these two problems and makes FIB technology more versatile for direct writing. The ion-beam resolution can now approach below 10 nm and thus ensures high precision in fabrication of nanostructures[30]. FIB direct-writing, via ion beam milling, implantation and ion induced deposition, is valuable for nanoscale fabrication, especially for prototyping devices.

Self-assembly

Self-assembly is a method using spontaneous organization and assembly of small components in a precisely ordered manner to yield larger objects with particular patterns and structures. In the nanoscale, self-assembly processes are bottom-up approaches to fabricate nanostructures and modify surfaces. These processes involve components or building blocks from the molecular to macro scale[31]. For example, self-assembled monolayers (SAMs) are molecular assemblies ordered by adsorption of to modify surfaces[32]. There are also structures that self-assemble from nanoparticles and block copolymers[33, 34]. Recent advances in the fabrication of functional structures using self-assembly include nanocrystals[35], magnets[36], micelles[37], microelectronics[38], 2D materials[39, 40], and even 3D functional structures[41, 42]with pre-designed building blocks.

2.2 FIB technology and applications

FIB has developed as an increasingly attractive technology in the field of materials characterization and micro/nanofabrication for both scientific research and industrial applications. It has the capability to characterize and fabricate 3D nanostructures by imaging, milling, ion implantation, and deposition[29]. FIB technology therefore has advantages such as wide availability, high accuracy, and reliability for nanoscale fabrication of complicated 3D structures.

A FIB system generally includes as main components an ion source, an optical column and a substrate stage in a vacuum chamber. Figure 1 shows a schematic drawing of a FIB system where a liquid metal ion source is utilized. Liquid metal film covers a refractory metal tip. Ions exactly at the sharp point of the tip are extracted and accelerated from the ion source by a potential difference. The upper lens on top of the ion column condenses the ions into a beam. The derived ions are filtered out to the desired ion species by a mass separator and restricted by a series of apertures. The ion beam coming out with a determined size is finally defined and focused by deflection octopole and objective lenses onto the sample surface.

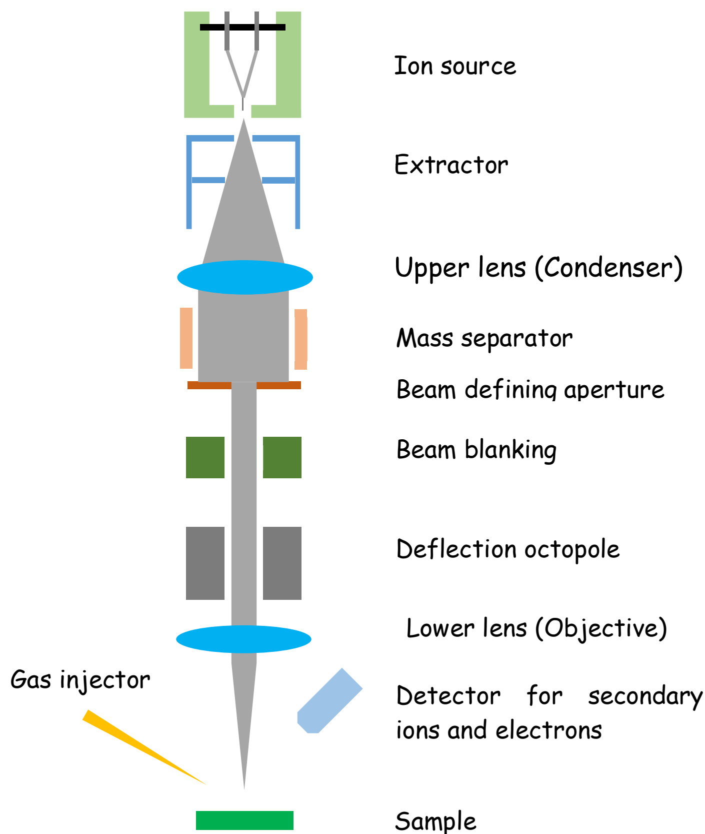

Figure 1. *Schematic diagram of a FIB system with a liquid metal ion source.*

Ion-solid interaction occurs when the focused and energetic ions collide with the sample surface. FIB causes ion implantation and generates secondary electrons and ions which can be detected for imaging. High-current FIB can not only selectively remove materials from the substrate by physical sputtering and ion-assisted chemical etching but also deposit materials on desired regions with the assistance of injection systems for precursor vapors.

The resolution of a FIB system is defined by the spot size on the target surface reached by the ion beam. The spot size is determined by the focusing capability of the ion column and the ion current. Higher ion current generally produces larger spot size and thus leads to lower resolution. Ion sources are critical for the success of FIB processing and will therefore be introduced next.

2.2.1 Ion sources for FIB instruments

Liquid metal ion source (LMIS)

Ion source is the heart of a FIB system and it determines the capability and performance of the instrument. It was not until LMIS appeared that FIB became a real technology. LMIS has the advantages of high current density, brightness and sputtering rates. It was originally applied to generate negative metal ions from target metal surfaces bombarded by positive cesium ions[43]. A cesium LMIS was designed for the first time in 1969 to produce single atom cesium ions from a capillary emitter by electrohydrodynamic (EHD) process with liquid metal of low work functions[44]. Ion beam from liquid gallium ion source was later found to have higher brightness and lower energy spread than that of cesium in EHD systems[45]. The first Ga^+ FIB system was established by Seliger et al. in 1978 with high current density and brightness in a 100 nm 57 kV probe[46]. Due to its low melting point and volatility, gallium has become the most widely used type of LMIS.

As the commercially most available LMIS, gallium ions have gained attention in many aspects, such as field-evaporation emission mechanism[47] and energy spread of ion beams [48, 49]. The energy spread increases with the emission current, which decreases the brightness and resolution of gallium ion beams. Space-charge close to the emitter and coulomb interactions in the ion beam are the main reasons for the energy spread in LMIS[50, 51].

Besides gallium, there are other elemental sources, such as bismuth and indium LMIS[52-54], which have been applied into FIB systems in order to get more ion species and also different beam sizes compared to gallium. The variety of ion species in FIB systems has been also increased by alloy LMIS which contains an eutectic binary or ternary alloy. Alloy LMIS can overcome the difficulty of directly utilizing specific elemental sources because the eutectic alloy has lower melting point and vapor pressure than the pure elements. The ion column is equipped with a mass filter for selecting the desired ion species so that the alloy LMIS has the advantage of maskless ion implantation of element which is one of the components of the alloy[55]. Large number of alloys have been investigated and developed

as ion sources in FIB systems for various applications. $Co_{36}Nd_{64}$ has been used to grow $CoSi_2$ nanostructures by Co implantation into Si and annealing[56, 57]. Au-Si-Pr alloy ion source has been developed for implantation of Pr ions into high-temperature superconductors[58]. Cu_3P ion source has been used as an n-dopant source for implantation of P ions[59]. $Dy_{69}Ni_{31}$[60] and $Au_{78.2}Dy_8Si_{13.8}$[61] alloys have been designed for implantation of Dy ions in order to create ferromagnetic structures in semiconductors. Ferromagnetic property has been also induced by Mn ion implantation into GaAs from an Au-Si-Mn alloy LMIS and subsequent annealing[62].

Gas field ionization source (GFIS)

GFIS is a field emission ion source which was firstly invented by Müller in 1951[63]. It is based on the principle that the applied electric field is large enough to extract an electron from a neutral gas atom and thus to produce a positive ion. GFISs were originally developed for imaging in field ion microscope (FIM) in 1950s[64]. FIM was the early stage of a field emission microscope which had the advantage of higher resolution than that of an electron microscope in the same period[65]. Helium was found to be the best gas for the high resolution ionized gases applied in FIM systems to study surface structures of metal (tungsten and rhenium) tips at an atomic level[64, 66].

It was not until 1975 when GFIS was applied to generate FIBs by a tungsten field ionization tip in a hydrogen atmosphere with a 200-nm resolution for scanning transmission ion microscope[67]. The available gas species for the GFIS are limited because of condensation at the required cryogenic temperatures. Helium has been well developed for imaging with a small virtual source size and energy spread[68]. Both small source size and energy spread of GFIS enable its sufficient brightness to be applied in FIB systems for imaging and nanomachining[68, 69]. However, the GFIS is not suited to high-rate milling tasks in FIB because of its low current density[70].

Plasma based ion sources

As compared to LMIS, plasma based ion source offers a wider variety of ion species and enables higher current FIB which is competent for higher processing yield and thus suits well for large volume milling. Various ion species, such as O_2^+, P^+, and B^+, have been used for maskless lithography[71]. However, the larger emission area of plasma ion source than LMIS results in smaller current density and thus smaller brightness of the plasma-based ion beam. The small brightness of the plasma ion source has been improved in inductively coupled plasma (ICP) ion source[72] and anode spot plasma (ASP) ion source[73].

For comparison of the three types of ion sources for FIB systems, Table 1 shows their differences in the aspects of ion species, beam spot size, energy spread, current density, beam brightness and applications. LMIS has become the choice for the commercial FIB systems because of proper beam size and brightness. GFIS has the smallest beam spot size and energy spread because the ions can be emitted from a single atom tip. For example, the

resolution of beams from helium GFIS (~0.5 nm) is better than that of gallium LMIS (~5 nm). FIB using inert gases has application advantages such as ability to image insulating samples. Plasma-based ion source has better beam purity and longer lifetime, but the large beam spot limits its applications to secondary ion mass spectrometry (SIMS) and fast and coarse milling. For example, the beam size of plasma based Xe^+ ions is almost 10 times larger than that of focused Xe^+ ion beam from GFIS. Xe^+ ion beam can mill substrates much faster than gallium ion beam, which is attributed to the larger mass of Xe^+ ions.

Table 1. *Comparison of ion sources used in FIB systems*

Ion source type	Ion species	Beam spot size (nm)	Energy spread (eV)	Current density (A/cm^2)	Beam brightness (A/m^2SrV)	Applications
LMIS[49, 74]	Ga^+, Au^+, Si^+, As^+, P^+ etc.	5-50	5-10	>1	10^6	Micro/nanofabrication, direct-writing, surface modification, TEM sample preparation
GFIS[75]	H_2^+, He^+, Ne^+, Ar^+, Kr^+, Xe^+	He<0.5,Ne~1, Xe,Kr~100[76]	~1		10^5	Ion imaging of insulating samples, nanomilling and nanodeposition
Plasma-based ion source	O_2^+, P^+, B^+, Ar^+, Xe^+, O^-	>1000[77]	1-3[78]	10^{-2}[72]	10^3-10^5[73]	SIMS, High-speed and large-volume milling

2.2.2 Basic functions and applications of FIB systems

FIB systems have four functions: imaging, milling, implantation and deposition. These are based on the ion-solid interaction between the incident ions and the target sample. The interaction causes electron emission, sputtering (both neutral and ionized atoms), and atom displacement in the solid sample, and chemical bond breaking. Therefore, FIB generates secondary electrons and ions which can be detected for imaging and high-current FIB can selectively remove materials from the substrate by physical sputtering. In addition, FIB causes ion implantation and deposition of materials on selected region by chemically decomposing precursor gas on the sample surface.

Imaging and characterization

When the ion beam is focused onto the sample surface, the accelerated ions interact with the surface atoms. This interaction generates secondary electrons that can be detected for imaging, which is called scanning ion microscope (SIM). The principle of SIM is similar to the scanning electron microscope (SEM)[79]. Spacial resolution of SIM is lower than that of SEM due to the more difficult focusing of ion beam than electron beam[80]. But the development of the FIB technology has led to an improvement of SIM resolution to 5 nm and better[81]. Compared to SEM, SIM has drawbacks of lattice damage of the target surface

and ion implantation into the specimen due to the energy transfer from the heavy ions. With the aid of FIB milling in the FIB/SEM and FIB/SIM systems, 3D tomography of nanostructured materials can be done by reconstructing images from a sequence of 'slicing and imaging' procedure[82].

Sputtered and then ionized atoms, resulting from the ion–solid interactions, can be analyzed by a SIMS[83]. SIMS thus has the capability to analyze the elemental composition of the ion-scanned surface and has applications in many fields such as geology, materials science and medical research. SIMS systems combined with FIB have been applied to get images of chemical composition and prepare site-specific specimen for SIMS analysis[84].

Milling

Along with the interaction of the ion beam with the target surface, the ions bombard the surface layer and remove the sample material which mills the substrate in precise regions defined by the ion beam scanning. The sputtered material from this physical milling process tends to generate redeposition which suppresses further milling. The milling rate depends on the sputtering yield which is determined by the target material, beam current, ion beam incident angle, and redeposition[80]. Milling is a top-down approach in terms of nanotechnology as material is stripped off from the solid sample locally without a mask. This approach has been widely used for fabrication of micro/nanostructures such as nanochannels[85], microcavities[86], trench templates for growth of carbon nanotubes[87], optical structures[88, 89] and nanosensors[90].

FIB milling can be used for patterning of various materials. For example, FIB milling of Au thin film on Si without any adhesion layer in between was used to define an array of Au nanoislands, see Figure 2. A tape peeling removed the Au layer except the nanoislands and plasmonic Au nanoparticles that had been fabricated. The redeposition on the sidewalls of nanoislands was utilized to protect them from the tape stripping[91]. In another study, FIB milling of a SiO_2 mask on Si was used for selective catalyst growth[92]. Gold grew on the FIB selected Si sites by a galvanic replacement reaction for the subsequent vapor-liquid-solid growth of Si nanowires. These Si nanowires were surface-oxidized to get core-shell Si/SiO_2 structures. FIB patterned the SiO_2 shell three dimensionally for defining branching points of special nanowires by a second material-selective catalyst growth followed by Si nanowire growth. FIB milling has also been used on 2D layered materials such as layer-by-layer thinning of MoS_2[93].

The application of gas injection into FIB systems enables gas-assisted etching by introducing a reactive gas during sputtering. The ion beam exites the gas molecules to react with the surface atoms of the substrate and thereby initiates the etching process on ion beam scanned areas. The gaseous byproducts are immediately pumped by the vacuum system, which reduces redeposition. This gas-assisted FIB milling largely increases the milling rate and has high selectivity to the substrate materials.

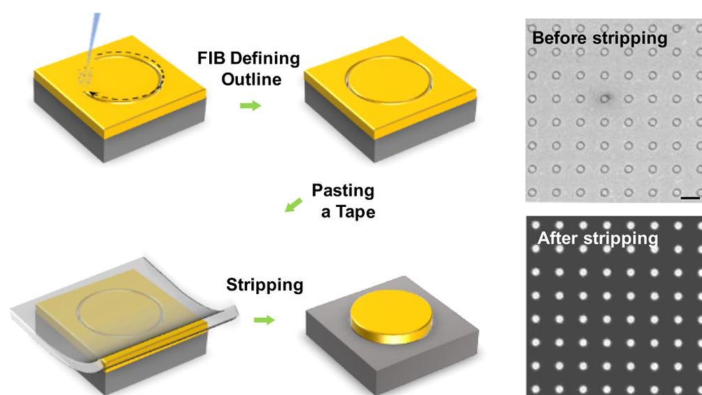

Figure 2. *Nanoparticles formed by FIB milling and tape peeling.*[91] *Reprinted with permission from (Y. Q. Chen et al, ACS Nano, 2016,* ***10****, 11228-11236). Copyright (2016) American Chemical Society.*

Ion implantation

When the ion beam interacts with the target, some ions are scattered on the target surface while others enter into the target with high energy, collide with target atoms, lose energy and finally stop inside the target. The implantation depth (ion range) is determined by the acceleration voltage, ion mass, and target material and orientation. The ion-beam parameters control the ion range and concentration in the target surface. Ion implantation is typically done with much smaller ion doses than the milling process. With FIB, the implantation can be done without masks for surface modification such as changes of electrical property, crystal structure and chemical reactivity. By contrast, in conventional implantation, masks are needed for good resolution.

The implanted ions can be dopants in semiconductors, for example, implanted gallium serves as a p-type dopant for the fabrication of silicon p-n junctions[94, 95]. Gallium ion implantation into In_2O_3 has been used to make transparent and conducting oxide nanowires. The electrical property changed because the implantation increased oxygen vacancy and carrier concentrations[96]. Ion implantation can also disorder crystal structures and thus change the properties of the crystalline materials. Helium ion beam has been used to direct write $YBa_2Cu_3O_{7-\delta}$ thin film with a 0.5 nm resolution to fabricate superconducting tunnel junctions[97]. That is because the ion implantation caused disorder or amorphization to the crystalline $YBa_2Cu_3O_{7-\delta}$ film that transited from a superconductor to an insulator at a proper ion dose. FIB implantation sometimes changes also the chemical property of the target. For example, gallium ion implantation into Au thin film has been applied for an improved catalyst system where ZnO nanowires grew with a narrower size-distribution and better vertical-alignment than Au catalysts without gallium implantation[98]. Ion implantation has been also used for fabrication of nanodots[99] and nanomasks[100-102] by selective etching of thin films where the implanted region was not etched. On the other hand, in some other cases, it is the implanted region that can be selectively etched for nanostructure fabrication[II].

FIB induced deposition

The application of gas injection into FIB systems also enables gas-assisted deposition which is also called ion beam induced deposition. When equipped with a precursor nozzle, FIB instruments have the capability to deposit materials on ion-beam-defined sites by means of chemical vapor deposition (CVD). The precursor vapors are sprayed and adsorbed on the sample in a vacuum chamber. The high-energy ion beam causes the adsorbed precursor molecules to decompose on the ion-beam-scanned area into nonvolatile material and volatile gases. The volatile byproducts are pumped out of the chamber while the nonvolatile material is deposited on the ion-beam-defined region of the sample surface. Combined with electron beam induced deposition in a SEM-FIB dual system, FIB induced deposition is widely used for making metal masks for TEM sample preparation. This bottom-up approach performs material addition also in nanoscale where the ion beam irradiates the target surface. Nanowires[103-106] and nanopillars[107, 108] have been successfully fabricated using this approach.

In summary, FIB technique has capabilities for research as well as industrial applications in various areas based on the four basic functions. Increasing amounts of different accessories, such as SEM and gas injectors, are added to FIB systems for optimized performance. For example, with the FIB/SEM dual beam system in our lab, using SEM for imaging protects the sample surface from ion implantation and gives a higher resolution as compared with ion-induced electron imaging. This combined system allows SEM imaging and simultaneously FIB micromachining, which enables *in situ* observation of FIB operation. Metal deposition on the sample surface is also available with a precursor gas injector and a focused electron or ion beam. Thus the advanced FIB-SEM dual beam system has high level of flexibility in diversified applications for micro- and nanofabrication of 2D/3D structures[29, 30, 109], TEM specimen preparation[110, 111], 3D topography[112, 113] and other applications in nanotechnology.

2.2.3 FIB-induced damage

In FIB processing, the charged and energetic ions collide with the solid sample. The ion-solid interaction causes a collision cascade and generates electron emission, particle sputtering, ion implantation and atom displacement in the solid sample. Figure 3 shows the ion-solid interaction between a 30 keV Ga^+ ion and a crystalline substrate. The implantation and atom displacement produce defects to the crystal lattice. As discussed in the ion implantation section, the intentional implantation is utilized to modify the sample surface, such as doping, or to enable further structure manufacturing. In other cases, however, the ion implantation and lattice damage are undesired but unavoidable and called implantation damage or ion-induced damage. The extent of the damage depends on the energy and incident angle of the ion beam, and material and structure of the substrate[114, 115].

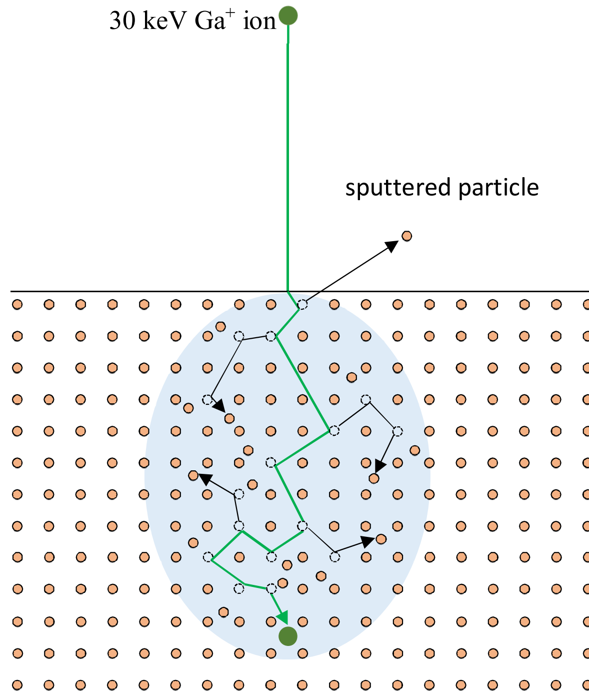

Figure 3. *Schematic illustration of a collision cascade generated by a 30 keV Ga^+ ion implanted into a crystal lattice, showing the ion implantation, atom displacement and the damage volume to the solid, drawn according to*[80].

There are simulation methods such as stopping and ranges of ions in matter (SRIM) and molecular dynamics for studying the ion-solid interaction and revealing the damage profile. There are also many experimental methods for evaluating the damage, such as TEM[116], surface resistance microscopy[117] and electron backscatter diffraction[118].

The ion-induced damage is the main concern for FIB applications, especially for the most common gallium focused ion beam systems. This damage generally involves both structural damage[119] and chemical contamination, and may cause considerable degradation of functional properties of the sample[120-122]. In the case of gallium implantation into crystalline silicon, both structural damage (amorphization) and degradation of thermal stability of silicon have been observed by SEM and TEM images. The degradation of the thermal stability is due to the segregation of gallium because of the poor solid solubility in the gallium-silicon binary system[123]. Many methods have been studied to reduce and minimize FIB induced gallium damage in crystalline silicon. Milling with a sacrificial metal layer is an effective method for reducing the ion-induced damage and to get well-defined sidewalls[85, 124]. Annealing treatment has been used for diffusion of implanted gallium atoms toward the surface and to enable recrystallization of the amorphized silicon[125]. However, the silicon surface turned rough after the annealing because of the segregation of gallium grains. Low-energy ion milling can be used for physically removing gallium

contamination while plasma etching[126] and wet etching[127] are chemical methods for partly removing the damaged layer.

The damage caused by FIB milling of silicon surface was studied in the first part of my work to improve the thermal stability of gallium FIB milled silicon surfaces. Oblique ion beam incidence and wet etching in KOH/H_2O_2 were found effective in this respect. ALD grown Al_2O_3 masks can also reduce the ion-induced damage and limit the damage to the sidewalls of FIB milled silicon trenches.

2.3 ALD in nanotechnology

Atomic layer deposition, originally termed 'atomic layer epitaxy'[128], is a thin film deposition technique which deposits thin films in a cyclic process. In one reaction cycle, a substrate surface is exposed to alternating pulses of two or more gaseous precursors and the precursor pulses are separated by inert gas purges which eliminate undesired gas-phase reactions and carry away excessive precursors and reaction byproducts. When the precursors are properly selected, their sequential pulsing leads to the saturation of both adsorption and reaction of the precursors in each cycle. Therefore, the thin film grows in a self-limiting manner and the film thickness can be controlled by varying the number of ALD cycles[129, 130].

The self-limiting growth mechanism in the ALD process results in the advantages of ALD thin films such as atomic level control of film thickness and composition, large-area uniformity, and excellent conformality. Taking these advantages of ALD, one can deposit ultra-thin films with excellent uniformity and conformality on large area substrates and also on 3D structures with high aspect ratios. The atomic level control of film thickness with sub-nanometer accuracy makes ALD a versatile approach in nanotechnology and nanofabrication[131-133]. This bottom-up technique has been employed for a wide range of nanotechnology applications such as electronic materials and devices[134-136], catalysts[137, 138], substrates for surface-enhanced Raman scattering (SERS)[139, 140] and energy technology materials[141, 142].

For ALD of thin films on organic nanostructures and biomaterials, lower deposition temperature and sometimes also precursor adjustments are required[143, 144]. Low-temperature deposition can also be realized by plasma enhanced ALD where the plasma activates one of the precursors and thereby improves the reactivity of that precursor[145, 146]. Area-selective ALD with the starting surface chemically modified enables localized deposition of thin films[147-149] and thus 3D nanostructures rather than planar thin films can be made by controlling the lateral dimensions of the selected deposition area. Because of its conformality, ALD can also make 3D nanostructures by depositing materials on 3D templates such as nanofibers and nanotubes[150-152].

2.3.1 Chemical composition control in ALD

ALD processes can deposit thin films of a large range of materials such as metals[153, 154], metal nitrides[155, 156], metal sulfides[157, 158] and metal oxides[159]. ALD of these materials in nanofabrication enables tailoring physical and chemical properties of the fabricated structures by tuning the chemical composition of the film and by modifying the surface of the fabricated structures.

ALD of metal oxides, including binary and ternary oxides, has been widely used in the field of microelectronics such as gate oxides, memory capacitors and ferroelectrics[129, 160, 161].

Mixtures and multilayered metal oxides have also been studied and applied with functionalized properties[162-164]. Metal oxide films can be deposited using different metal precursors such as halides, alkoxides, alkylamides and cyclopentadienyls[129, 159, 165].

There are examples of ALD for surface modification and chemical composition control for nanoscaled catalysts. Ultrathin (~1 nm) ALD Al_2O_3 thin films were annealed to form Al_2O_3 nanoparticles serving as catalysts for carbon nanotube growth[166]. Catalytic nanorockets have been made by ALD of TiO_2 on a template with cylindrical pores for nanotubes and ALD of Pt inside the nanotubes[167], shown in Figure 4. The hollow Pt/TiO_2 nanotubes were set free from the template with one end open. The Pt-coated inside wall of the TiO_2 tube catalyses the decomposition of H_2O_2 and generates an O_2 gradient. The O_2 gradient drives the nanotubes towards the direction of their sealed ends. Dual photocatalysts for hydrogen production from water have been made by ALD of Pt and CoO_x nanoclusters on porous TiO_2 nanotubes[168]. The high photocatalytic activity of the dual catalysts derives from the highly dispersed Pt and CoO_x nanoclusters made by one cycle ALD processes. The CoO_x acts as a hole collector and thereby separates the photogenerated electrons and holes. In another study, Co_3O_4 nanotraps were fabricated for Pt nanoparticle catalysts with improved thermal stability and catalytic activity[169]. Area-selective ALD of Co_3O_4 was performed on 1-octadecanethiol (ODT) treated Pt nanoparticles on Al_2O_3 support to grow Co_3O_4 only on the Al_2O_3 surface while the Pt nanoparticles were protected by ODT.

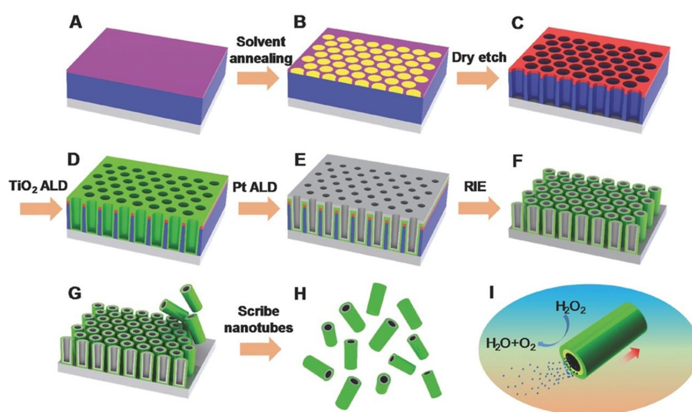

Figure 4. *Schematic drawing of nanorocket fabrication by ALD of TiO_2 and Pt on a nanopore template, reactive ion etching, and lift-off to form TiO_2/Pt catalyst nanotubes. The nanotubes move towards their sealed ends, driven by the O_2 gradient caused by the decomposition of H_2O_2. Reprinted with permission from (J. Li et al, Adv. Funct. Mater., 2017, **27**, 1700598). Copyright (2017) WILEY-VCH Verlag GmbH & Co. KGaA, Weinheim.*

ALD grown ultrathin films have also been used for diffusion of one material into another one upon annealing treatments. For example, Al_2O_3/ZnO/Al_2O_3 multilayers grown by ALD at low temperature on fiber templates were used for diffusion of ZnO into Al_2O_3 to get $ZnAl_2O_4$ tube-in-tube structures after annealing[170]. Elemental doping can be realized by ALD of metal oxides and heating for diffusion of the metal element, such as diffusion of

zinc from a ZnO ALD film to get Zn doped GaP[171], Ti diffusion into Fe_2O_3[172], Mn doped in TiO_2 nanowires[173] and Bi doped in silicon[174].

Residual impurities are always a concern of ALD thin films. The impurities come from the precursors because of the incompleteness of the reactions. The impurity concentrations of ALD grown thin films can be decreased by optimizing the deposition temperature[175]. In addition, the crystallization of ALD grown thin films can be controlled by deposition temperature and is also dependent on the impurity contents. Crystallinity of the films can generally be improved by annealing[176].

2.3.2 Dimensional control in ALD

Size is another important factor that affects the properties of nanomaterials, besides composition. Nanomaterials of the same substance exhibit size-dependent properties such as color and reactivity. Thickness control of ALD thin films at a sub-nanometer level is achieved easily by changing the number of deposition cycles, because of the self-limiting and layer-by-layer growth mechanism of ALD process. So the dimensional control of the resulting thin films is inherent when the ALD process is well designed.

The dimensional control by ALD is utilized for pattern multiplication in nanoscale lithography[133, 177-180]. The pattern multiplication doubles the feature density and improves the spatial resolution with ALD thin films serving as spacers or sidewalls, see Figure 5. The equal thickness of the sidewalls results from the conformality of ALD thin films and it can be easily tuned to the desired linewidth for nanofabrication. The frequency doubled patterns can be used as etch masks and imprint templates. These patterns can also be doubled once more to quadrupled patterns with even smaller dimensions.

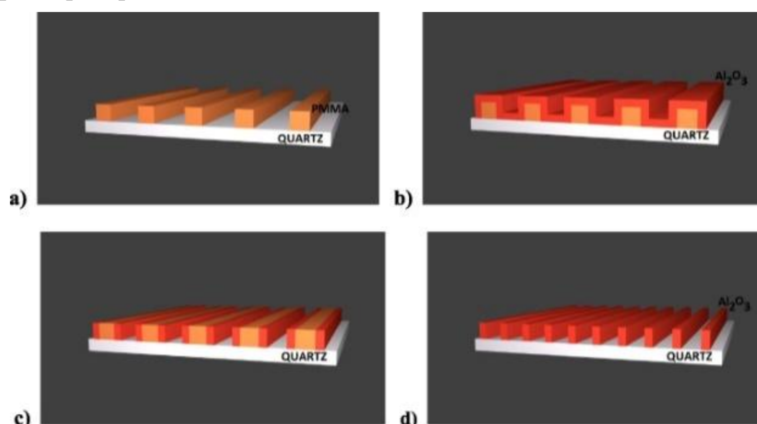

Figure 5. *Schematic illustration of pattern multiplication by ALD of Al_2O_3 on a poly (methyl methacrylate) (PMMA) pattern and etching away of lateral Al_2O_3 followed by complete removal of PMMA. The frequency or feature density of the pattern gets doubled in this process. Reprinted with permission (from C. Dhueyet et al, Nanotechnology, 2013,* ***24****, 105303). Copyright (2013) IOP Publishing Ltd.*

The dimensional control and conformality of ALD are also extremely important and useful for fabrication of various 3D nanostructures. For example, ALD ZnO film has been applied as a seed layer for the growth of ZnO nanowires with an ultrathin ALD TiO_2 layer partially blocking nucleation on the ZnO seed layer, see Figure 6(a). The ultrathin TiO_2 layer does not have a complete coverage and leaves holes for the nucleation of ZnO nanowires. The thicknesses of the ZnO seed layer and TiO_2 layer control the orientation and density of the ZnO nanowires[181]. After second and third rounds of ALD of seed and blocking layers and nanowire growth, branched ZnO nanowires are formed and the surface becomes superhydrophobic. The dimensions and properties of the surface can be precisely tuned by the cycle numbers of ALD seed and blocking layers[182], see Figure 6(b) and (c).

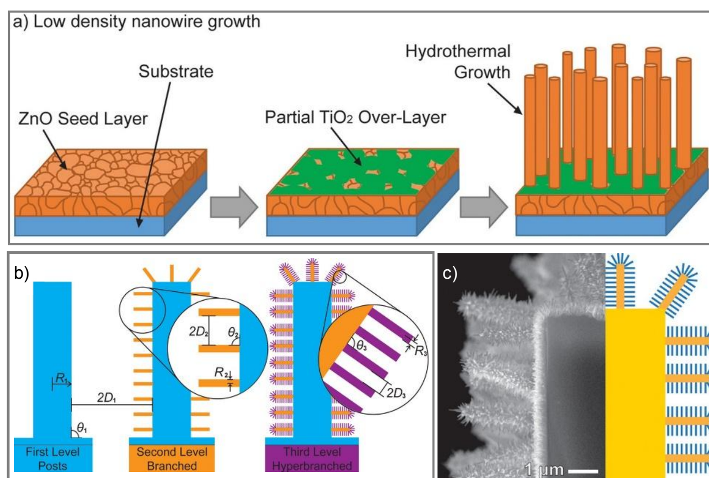

Figure 6. *ALD of ZnO seed layer and TiO_2 blocking layer for the growth of branched ZnO nanowires. A superhydrophobic surface is achieved by repeating the ALD of ZnO seed layer and TiO_2 blocking layer and nanowire growth resulting in branched structures. Reprinted with permission from (A. R. Bielinski et al, ACS Nano, 2017,* ***11****, 478-489). Copyright (2016) American Chemical Society.*

ALD cycle numbers determine wall thicknesses of hollow structures formed by conformal coatings on nanotubes[183], nanowires[168] and polymer templates[152, 184]. When the starting template has special structures such as nanopores, the precise dimensional control of ALD becomes significant for controllable narrowing and even filling of the pores with conformal coating on their inner surfaces[185-187]. The size of the empty space can be tuned by simply changing the number of ALD cycles. Ultrathin ALD oxides have also been used as sacrificial layers for formation of nanogaps in metal films for optical applications[188] and for SERS[189].

ALD is a perfect technique for deposition of thin films composed of ultrathin and uniform layers of different materials with precise thicknes. ALD of nanolaminates utilizes both the compositional and dimensional control of the ALD technique. The properties of the nanolaminates depend on the materials and layer thicknesses of the laminated stack. For

example, optical properties of Al_2O_3/ZnO nanolaminates changed with the bilayer thicknesses[190, 191]. Dimensional control of the ALD technique was also utilized for making highest resolution Fresnel zone plates for x-ray microscopy[192, 193] with tunable zone materials and widths. Pt/In alloy nanoparticles have been made for catalytic application by ALD of In_2O_3 and Pt with a cycle sequency m*(x*In_2O_3+y*Pt) and a reduction treatment[194]. The particle size was tuned by controlling the total thickness(m) of Pt/In_2O_3 layers when the x and y were fixed, and the alloy phase composition was tuned by the In_2O_3/Pt ratio (x/y). The authors made similarly also Sn/Pt alloy particles with ALD of SnO_2 and Pt films by precisely controlling the thickness of each layer[195].

3 Experimental

3.1 Structure fabrication

Silicon <100> wafers were used in all experiments. SiO_2 films were prepared by thermally oxidizing (1000 °C) of silicon<100> wafers in air. Metals were deposited on various samples by electron-beam evaporation. Annealing tests were performed in a Carbolite Tube Furnace under N_2 atmosphere at 250 °C to study thermal stability of FIB milled surfaces.

Al_2O_3 and Ta_2O_5 thin films were deposited by ALD in a Picosun SUNALE R-150 flow type reactor at 250 ºC utilizing trimethylaluminium (TMA) + H_2O and $Ta(OEt)_5$ + H_2O as precursors, respectively. Film stacks of $Al_2O_3/Ta_2O_5/Al_2O_3$ were deposited on Si, SiO_2/Si and Au/SiO_2/Si substrates in an F-120 reactor. The samples were cleaved to small pieces for FIB patterning and wet etching. The milled structures were aligned to the crystal structure of silicon by aligning the FIB patterns parallel to the cleaved specimen edge. ALD growth of Ta_2O_5 thin films on FIB milled and wet etched SiO_2/Si structures was performed with extended purges in order to completely remove vapors of byproducts and precursors from the narrowed openings of the channels to be formed.

FIB milling was performed in an FIB-SEM dual beam system (FEI Quanta 3D 200i) with 30 keV focused gallium ions. A 100 pA beam current was used for oblique milling and the ion incident angles were changed by using the stage tilting and pre-tilted sample holders. A 300 pA beam current was used for milling silicon with 10×10 μm^2 squares for thermal and etching experiments. 30 pA ion beam was used for single-pass scanning for implanting nanodot arrays with 200 nm X and Y pitches and a dwell time/dot 5.0 ms. When FIB milling on insulator mask materials, for example Al_2O_3 or SiO_2, a 30 keV gallium ion beam with 100 pA current and 90 % overlap was applied and the electron gun in the dual beam system was used for charge neutralization to suppress drifting.

KOH/H_2O_2 Etchant (1mol/L:1mol/L) was used at room temperature to remove gallium rich silicon surface immediately after FIB milling and implantation. Micro- and nanostructures (nanopore arrays and nanotrenches) were fabricated with this removal process. For the nanotrench formation, two more etching steps were applied after the KOH/H_2O_2 etching. 1 % HF was used to remove the rest of the implanted surface and the native oxide on silicon and 1 mol/L KOH to etch silicon through the FIB openings in SiO_2. 1 mol/L KOH was also used to etch and release FIB-milled $Al_2O_3/Ta_2O_5/Al_2O_3$ on silicon for nanowire formation. FIB-milled samples with $Al_2O_3/Ta_2O_5/Al_2O_3$ on SiO_2 were etched in 5 % tetramethylammonium hydroxide (TMAH) at 50 °C to remove Al_2O_3 from FIB openings for making 2D and 3D Ta_2O_5 masks and to realize the lift-off of the 2D mask after metal evaporation. All the etching reactions were stopped by moving the sample from the etchant and rinsing it twice in DI H_2O, and soaking in DI H_2O for 10 min followed by drying the sample with a N_2 gun.

3.2 Analysis and characterization

The surface morphology was studied by SEM and STEM images collected in the dual beam system and FESEM (Hitachi HiTech S-4800). Cross-sectional TEM images of interesting sites were taken in a FEI Tecnai F20 (200 keV) instrument. Specimens for the TEM and STEM imaging were prepared with the dual beam instrument by the lift-out method[110].

Surface imaging for depth and roughness measurements was done using an AFM (Veeco Multimode V) instrument in air in a tapping mode. FIB milled, wet etched and post-annealed square trenches were imaged with soft silicon probes (tip radius 8 nm and spring constant 3 N/m). The surface roughnesses of the bottoms of trenches were calculated as root-mean-square values (Rq). Sharpened silicon probes (tip radius 2 nm and spring constant 40 N/m) were used for imaging nanopore arrays. Image processing and analysis were done using a Bruker Nanoscope Analysis 1.5 program.

The compositions of the as-milled squares prepared with different incident angles and the effects of gallium removal were measured by energy-dispersive x-ray (EDS) analysis with a Xmax 50 mm^2 SSD detector and an Oxford Instruments Inca 350 analyzer. EDS measurements were done with 3-5 keV acceleration voltage in order to achieve sufficient surface sensitivity.

Time of flight elastic recoil detection analysis (TOF-ERDA) was used to measure the elemental distribution of FIB milled and wet etched square surfaces. 1.2 ×1.2 mm^2 squares were FIB milled by a 30 keV, 50 nA ion beam with an ion dose of 8.34×10^{16} $ions\cdot cm^{-2}$. 40 MeV $^{127}I^{9+}$ primary ions were obtained from a 5 MeV tandem accelerator[196] for the TOF-ERDA depth profiling. The angle of recoil detector was 40 ° and the angle of the sample surface was 20 ° to the incident beam.

4 Results and discussion

The main experimental results are described in this section. Detailed results and more thorough discussion can be found in the corresponding publications Ⅰ-Ⅳ. This section contains also some new results that have not been published earlier.

4.1 Thermal stability of FIB milled silicon surfaces

As discussed in Section 2.2.3, FIB is a versatile tool for nanostructure fabrication, but it suffers from the ion beam induced damage to the target surface. ALD processes are typically performed at 200-500 °C, which makes the thermal stability a critical issue for combining FIB direct-writing and ALD. So the thermal stability of gallium FIB milled silicon surface was studied prior to studying the feasibility of combining FIB and ALD in nanofabrication on silicon surface[I].

Although the as-milled features are smooth, the top view of these features after annealing for 30 min in N_2 at 250 °C showed significantly rougher surface (Figure 7). Gallium segregation and surface roughening took place not only on the milled structure but also on the surrounding surface as the gallium implanted silicon layer is metastable and changed upon heating. The observed segregation and roughening result from the lack of a stable gallium silicide phase. In the gallium-silicon binary system, gallium solubility is quite low, around 0.1 atomic percent[123]. Surface diffusion of gallium from the FIB milled trenches to the surroundings was studied by Mikkelsen et al. who also observed the spreading of gallium from the milled areas upon heating to 150-200 °C[197].

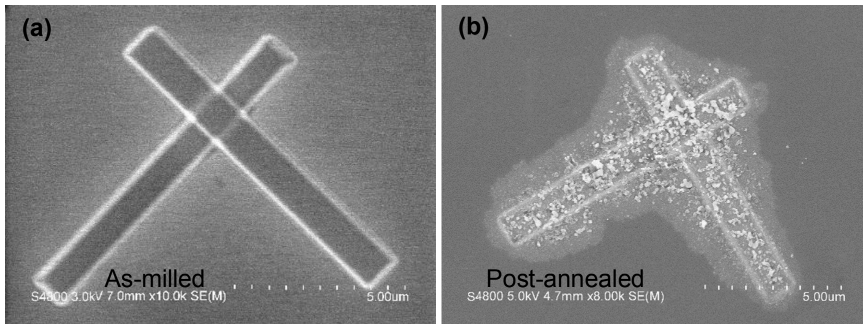

Figure 7 *SEM images of (a) as-milled structure (1 μm×10 μm cross 1 μm ×10 μm) on silicon by 30 keV 100pA FIB, ion dose 4.2×10^{17} ions·cm^{-2} (b) surface post-annealed in N_2 at 250 °C for 30 minutes.*

4.1.1 Oblique incident ion beam

Ion-beam incidence angle (0° is defined here as the normal of the target surface) was changed to decrease the amount of implanted gallium. A 10 µm × 10 µm square pattern was defined for the oblique milling with 30 keV, 100 pA ion beam. The actual milling area on the silicon surface gets elongated along the ion beam tilting direction. The sputtering yield increases with the ion beam incidence[198]. The ion dose per area was kept constant at 4.2×10^{17} ions·cm^{-2}, which results in a deeper milling depth at higher incident angles than that at normal incidence. As seen in Figure 8, the thermal stability of the FIB milled surface gets dramatically improved when the incident angle increases. Surfaces milled with perpendicular beam at 0° angle and annealed at 250 °C show strong segregation. There is less segregation on the surface milled by 20° tilting compared to the 0° tilting. 40° tilting decreased segregation in the milled area and the surrounding surface further, but the milled area still becomes very rough with small particles upon annealing. The surface milled at 60° angle is generally smooth, and roughening takes place only at the lower edge where the ion beam scanning started and direct implantation occurred. For the largest glancing angle of 80°, the annealed trench surface is quite smooth and thus thermally stable.

The SRIM simulation in Figure 8(b) shows the distribution of implanted gallium ions in silicon. The inset numbers are simulated ion ranges describing the projected range of the maximum concentrations of implanted ions. The gallium ions penetrate less deep into the silicon substrate with higher incident angles even though the implanted length stays the same. Shallower implanted gallium ions are easier sputtered out to the vacuum during milling. The damage volume is even smaller for 60° incidence and smaller still for 80°, because some of the incident ions are scattered away from the surface.

The results of the oblique incidence milling suggest that milling at 60° and higher incident angles provides a means for making thermally sufficiently stable structures such as square trenches and V-shaped grooves, with the undesired effects limited to the very end of the milled structures. Most studies on gallium implantation deal with milling at high incident angles such as 80-90°, for example in the case of TEM sample preparation. These high incident angles are difficult to use in prototyping, as the surface field-of-view is limited and shadowing by any topography is severe. The study in this case takes 60° as the optimized incident angle for sufficient thermal stability of milled silicon surface by a 30 keV focused gallium ion beam.

Figure 9 shows gallium and silicon signals from EDS measurements of as-milled surfaces with different angles of incidence. Silicon and gallium peaks in Figure 9(a) reveal the angle dependence of gallium concentration implanted into silicon. The gallium concentration decreases and surface silicon concentration increases along with the angle of incidence. k-ratios of gallium and silicon from the EDS measurement in Figure 9(b) show also that the concentrations of gallium and silicon change as a function of the angle of incidence (0-60°).

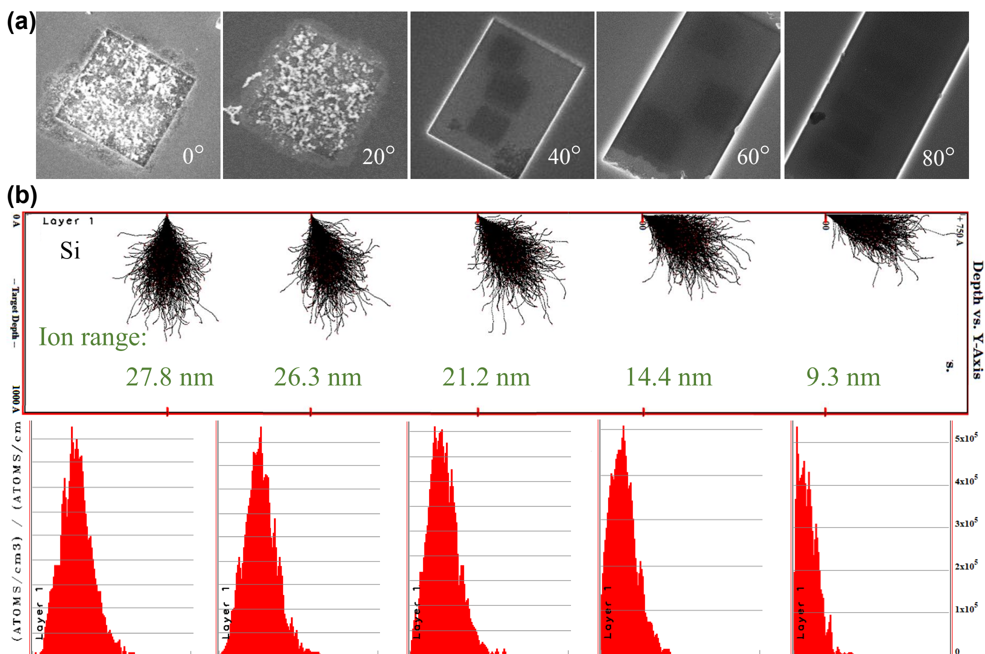

Figure 8 *(a) FESEM images of post-annealed surfaces milled at incident angles 0°, 20°, 40°, 60° and 80°. All features were milled using a 10 µm×10 µm pattern. The ion dose was kept at 4.2×10^{17} ions·cm^{-2} and the annealing was performed for 30 minutes at 250 ℃ in N_2. The small darker contrast squares inside the boxes 40° and 60° are formed by surface contamination during EDS measurements. (b) SRIM simulation of 30 keV gallium implantation into silicon substrate and the depth distribution of implanted ions with the corresponding angles of incidence.*

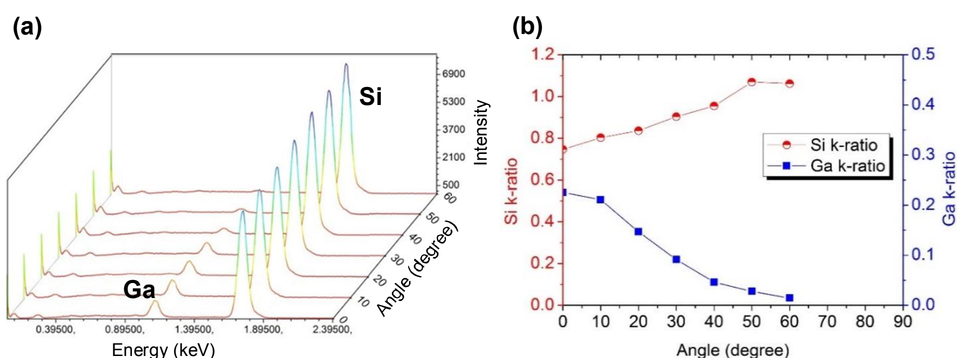

Figure 9 *(a) EDS spectra and (b) k-ratios of Si and Ga for different incident angles of gallium milling of silicon by 30 keV FIB with a dose of 4.2×10^{17} ions·cm^{-2}. Measurements are from the as-milled surfaces with a 5 keV electron probe for sufficient surface sensitivity for the thin gallium-implanted layer.*

In order to study the compatibility of ALD with the FIB milled features, a 20 nm thick Al_2O_3 film was grown with TMA and H_2O as precursors at 250 °C. The deposition temperature was the same as in the previous annealing experiments. Figure 10(a) shows a TEM image of an ALD Al_2O_3 film grown at 250 °C on a Si surface milled at 0°. Al_2O_3 thin film has grown on the FIB-milled surface with a uniform thickness regardless of segregation during heating to the ALD temperature. The amorphous oxide makes the final surface smoother than the annealed only surface.

Trenches were milled also with a 60° incident angle to make thermally stable trench surfaces for the ALD of thin films. Figure 10(b) shows a cross-sectional image of an ALD Al_2O_3 film grown on a narrow trench formed by FIB milling at a 60° incidence. The Al_2O_3 thin film was found to grow conformally with a 20 nm thickness on the trench surface. No substrate changes due to heating the sample to the ALD process temperature were observed. Compared to the 0° milled surface in Figure 10(a), the 60° milled silicon surface is thermally more stable after ALD at 250 °C. ALD on the narrow trench in Figure 10(b) was found a method for filling and/or controlled narrowing of trenches. Nanoscale structures can be easily achieved ALD narrowing given structures with ALD Al_2O_3 or other materials.

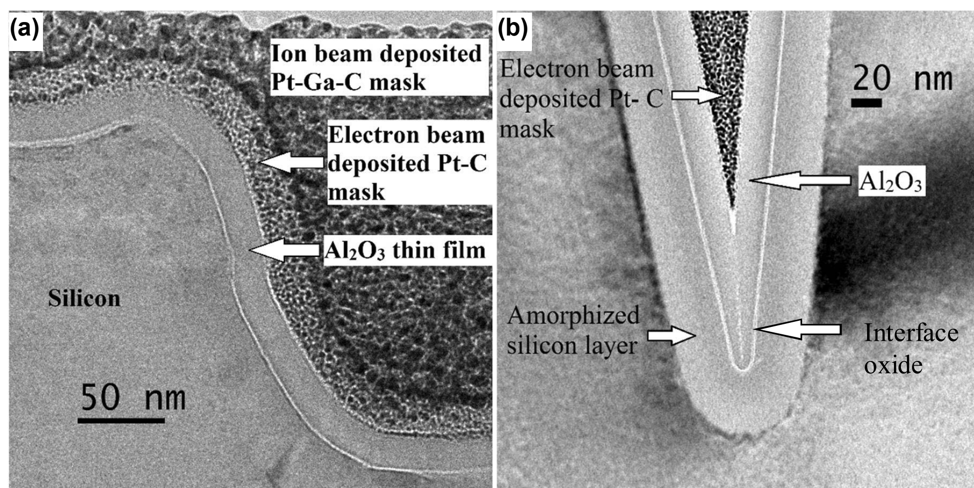

Figure 10 *Cross-sectional TEM images of (a) the edge of an area which was milled at 0° and then coated with ALD Al_2O_3 at 250 °C. (b) ALD of Al_2O_3 on a V-shaped trench made by FIB milling with 30 keV, 50 pA ion beam at 60° incident angle.*

As a summary, ALD Al_2O_3 thin films were found to grow conformally on the gallium milled silicon surface in both cases, even when the surface segregation occured (0° milled) due to the heating of the sample to the ALD process temperature. The direct use of FIB milled silicon as a template for ALD is improved when the gallium implantation is minimized by decreasing the beam incident angle to 60°. ALD of Al_2O_3 thin films could be used both for controlled narrowing of FIB milled trenches and for creating a chemically uniform and good starting surface for ALD process of other materials.

4.1.2 Wet etching by KOH/H_2O_2

As seen in Section 4.1.1, FIB milled silicon suffers from segregation of metallic gallium and irreversible surface roughening after heating, which results from the metastable gallium-rich surface after the FIB milling. This motivates to study the removal of the gallium implanted layer at room temperature by a proper etchant. Chemical wet etching was studied and a KOH/H_2O_2 solution was found to be an effective etchant[II].

The gallium-rich surface contains gallium as a metastable alloy or oxidized metal. In order to remove the gallium-rich surface, an etchant must react with both metallic and oxidized gallium. KOH is a widely used anisotropic etchant for silicon and has a much lower etching rate for SiO_2. Etching of metallic gallium (99.99 %) and Ga_2O_3 powders (≥99.99 %) was tested first in separate test tubes with 1 mol/L KOH solution at room temperature overnight. The results showed that Ga_2O_3 is dissolvable but the dissolution of metallic gallium is very slow, because only in Ga_2O_3 the oxidation state +ɪɪɪ of gallium is the same as in the complex anion $[Ga(OH)_4]^-$ that is the predominant species of gallium in strong basic solutions[199]. So an oxidizer is needed to improve the dissolution of metallic gallium. H_2O_2 was chosen because of its oxidation power, low toxicity and sufficient stability in basic solutions at room temperature.

Figure 11 demonstrates how the adding of H_2O_2 affects the KOH etching of gallium-implanted silicon. A square pattern (10 µm × 10 µm) was FIB milled on silicon with ion doses 2.09×10^{17}, 4.17×10^{17} and 8.34×10^{17} ions·cm^{-2} from the top down, shown in Figure 11(a). The milled sample was then treated with 1 mol/L KOH at room temperature for 3 hours, shown in Figure 11(b). The KOH solution anisotropically etched silicon in the surrounding area while the implanted area with gallium ions above the masking threshold doses had a masking effect for the etching. Figure 11(c) shows FIB milled squares treated by KOH/H_2O_2 solution (1 mol/L:1 mol/L). The KOH etching of the surrounding area is suppressed by the added H_2O_2 which oxidizes the silicon surface to SiO_2 which serves as an etching mask in KOH solutions. The etching of the FIB milled squares by KOH/H_2O_2 was detected by low energy EDS measurement shown in Figure 11(d). There is a dramatic decrease of the surface gallium content in the FIB milled squares after etching at room temperature for 3 hours. It is proposed that in the FIB milled area the amount of gallium in the surface oxide layer (oxidized by H_2O_2) is high enough to make it soluble to the etchant while the surrounding oxidized silicon surface is stable against etching. So the added H_2O_2 oxidizes both gallium and silicon on the surface, which makes the implanted gallium dissolvable and dramatically suppresses anisotropic etching of silicon by KOH.

The etching process of KOH/H_2O_2 (1 mol/L:1 mol/L) on FIB milled squares and their thermal stability were studied by SEM and AFM measurements. SEM images in Figure 12(a) show the FIB milled 10 µm x 10 µm features as-milled and etched for 0.5, 3 and 6 hours in KOH/H_2O_2, while Figure 12(b) shows the corresponding surface morphology from the AFM measurements. The surface roughness R_q is increased for the half hour etched square due to the removal of gallium from the milled surface, but begins to decrease as the etching

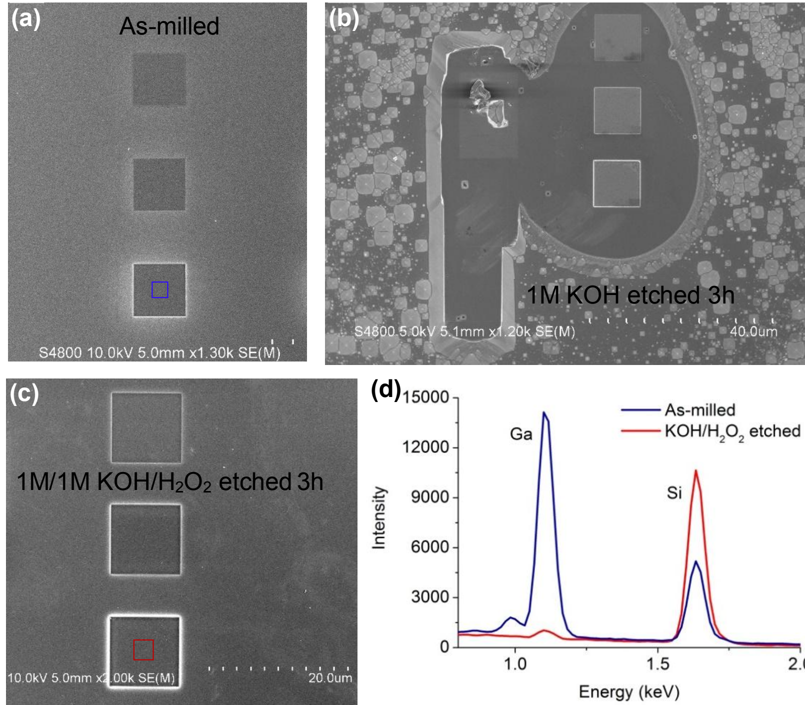

Figure 11 *SEM images of (a) as-milled 3 squares by ion doses 2.09×10^{17}, 4.17×10^{17} and 8.34×10^{17} ions·cm^{-2}, respectively, (b) milled and anisotropically etched silicon surface in 1mol/L aqueous KOH and (c) milled and etched silicon surface in the KOH/H_2O_2 solution and (d) low-energy EDS measured from highest-dose sites shown in (a) and (c).*

goes further. After annealing the samples in N_2 at 500 °C for 10 min, a clear change in the thermal stability due to the wet etching is seen in Figure 12(c) and the corresponding change in surface roughness is seen in Figure 12(d). After annealing, the milled only surface suffers from segregation and the roughness R_q is 70 nm, whereas wet etching effectively eliminates the segregation and the surface roughness is reduced to less than 1 nm in the sample etched for 6 hours. The removal of the implanted gallium and the improvement of the surface stability make it much more reliable to apply subsequent processes which require heating of the FIB milled samples, such as physical vapor deposition (PVD), ALD and chemical vapor deposition of thin films.

It is very interesting and important to note the self-terminated nature of the etching process. Square trenches were patterned by FIB milling with three different ion doses, 2.09, 4.17 and 8.34×10^{17} ions·cm^{-2}. Figure 13(a) shows how the depth values were derived from the AFM measurements while Figures 13(b) and (c) show depths of the square trenches and roughnesses of the bottom surfaces, respectively, as a function of etching time in KOH/H_2O_2. With all doses, the depths of the square trenches increase during the etching process but eventually they reach stable values. The total increase of the depth is in the range of 25-30

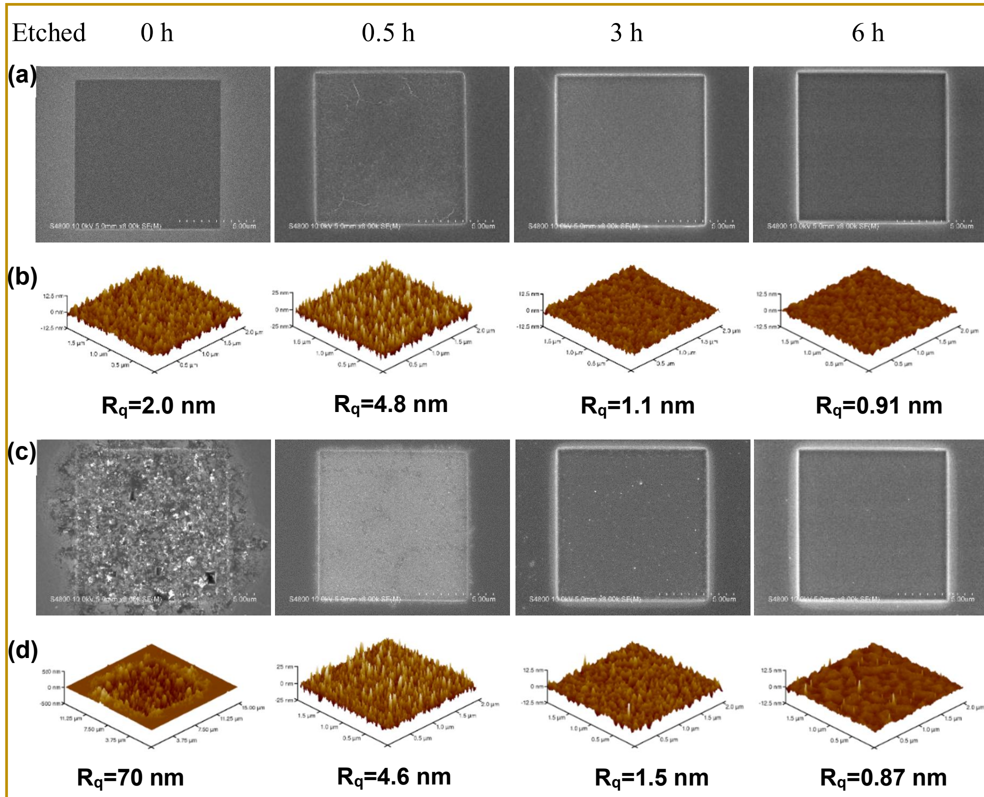

Figure 12 *(a) SEM and (b) AFM images of milled squares in silicon followed by wet etching in KOH/H_2O_2 solutions for 0 h, 0.5 h, 3 h and 6 h respectively. (c) SEM and (d) AFM images of post annealed squares on as-milled and etched samples. The milling ion dose for the squares was 4.17×10^{17} ions·cm^{-2} and the sample annealing was performed in N_2 at 500 ℃ for 10 minutes.*

nm after 6 hours of etching, independent of the ion dose. A SRIM simulation of the depth distribution of gallium ions implanted into silicon gave as the depth of the maximum concentration 27.8 nm for 0° milling with 30 keV ions, seen in Figure 14. This depth is similar to the observed increase of the trench depth after etching for 6 hours. The final surface roughness of the trench bottom varies in the range of 0.5-1.0 nm for all the three ion doses after 6 hours of etching. The smoothest bottom surface was obtained with the highest milling ion dose, which is attributed to the most uniform gallium implant layer where the influence of single ion event is averaged out.

As seen in the results of the depths and roughnesses of the etched surfaces, the wet etching by KOH/H_2O_2 became self-terminated after 6 hours when about 30 nm of the bottom surface of the implanted trench was removed. This leaves gallium residue in the silicon because according to the SRIM simulation the maximum penetration depth of gallium is twice more

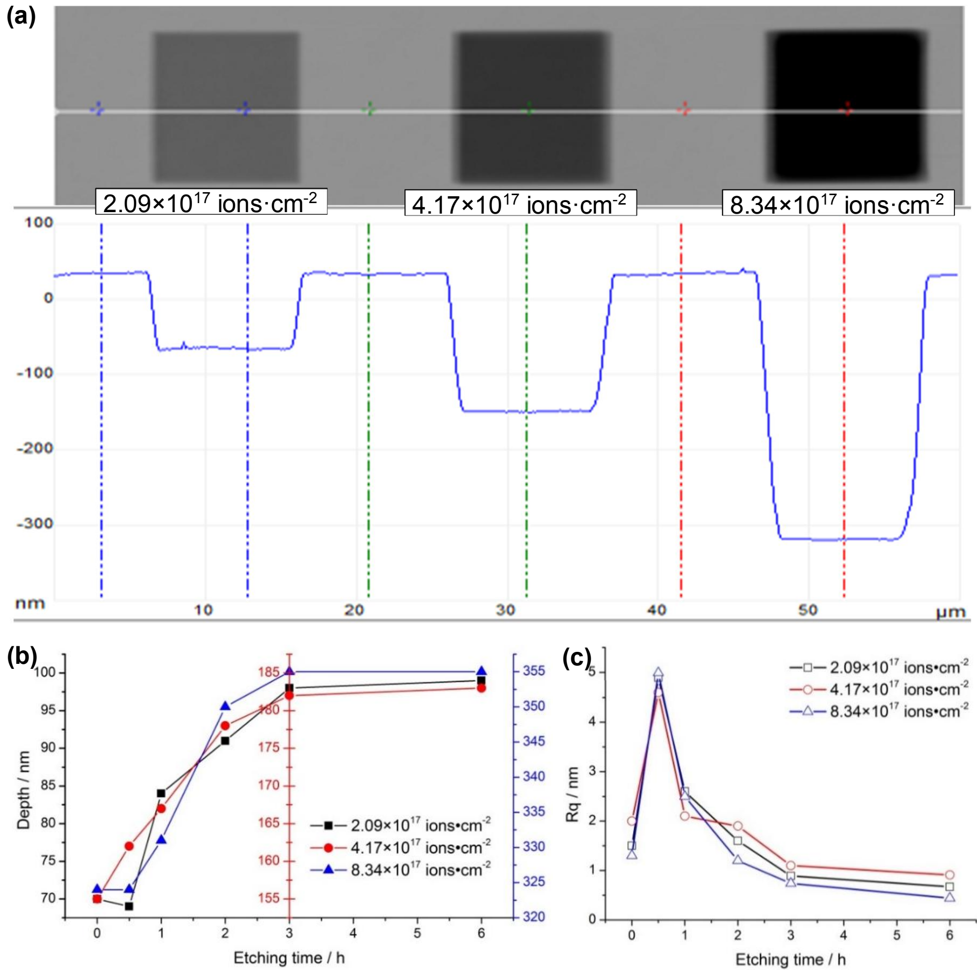

Figure 13 *(a) AFM depth measurement of squares milled by 30 keV, 0.3 nA gallium FIB with different ion doses:* 2.09×10^{17}*,* 4.17×10^{17} *and* 8.34×10^{17} *ions·cm*$^{-2}$ *(b) depths and (c) surface roughness* R_q *values of FIB milled and wet etched squares produced by various milling doses and with different etching times.*

than the removed depth. In order to understand what suppresses further etching for removing the entire implanted volume, ERDA measurements were done to study the changes of elemental depth distributions during the etching process. A 30 keV, 50 nA ion beam was used to mill a large area (1.2×1.2mm^2) with an ion dose 8.34×10^{16} ions·cm^{-2}. The large area is necessary for the ERDA measurements.

Figures 15(a)-(c) show depth profiles of gallium, oxygen, hydrogen and carbon after wet etching for 20-180 min, while Figure 15(d) compares the depth distributions of gallium in the three samples. The concentration of gallium decreases due to the interface moving deeper along with the etching time. The concentration change of oxygen is much less than

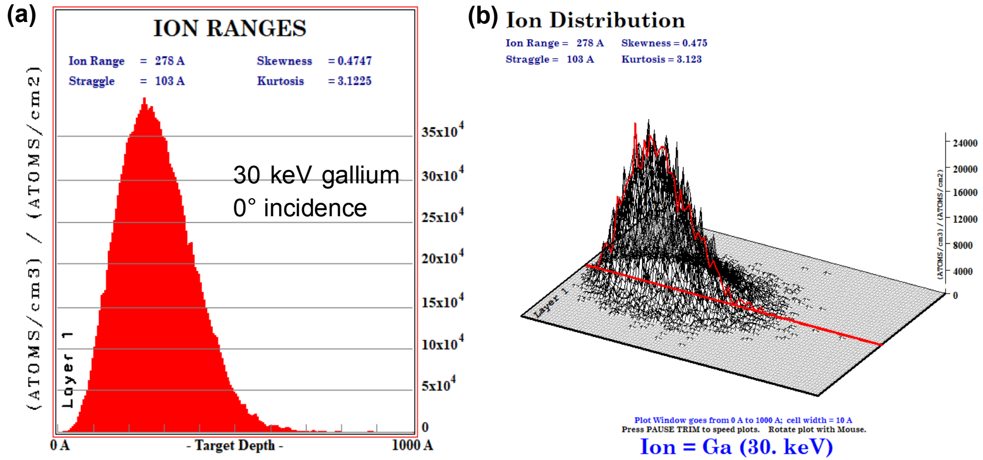

Figure 14 *(a) Ion range and (b) 3D ion distribution from SRIM simulation of gallium implanted into silicon by a 30 keV voltage, 0° incident ion beam.*

that of gallium and thus the concentration of gallium on the near surface gets lower than that of oxygen in the 180 min etched sample. The low concentration of gallium in a thin Si-Ga-O layer means that SiO_2 fraction is high enough for resisting further dissolution. As discussed before, SiO_2 suppresses KOH etching of silicon in presence of H_2O_2. Therefore, the formation of the SiO_2-rich layer explains the etch-stop effect observed in Figure 13(b) and prevents complete removal of the gallium residue in the KOH/H_2O_2 solution. On the other hand, the gallium residue remaining after 180 min etching is mainly located within the Si-Ga-O surface layer (Figure 15(c)). Gallium is more stable in Si-Ga-O than in silicon and therefore does not cause segregation and roughening.

This study has demonstrated that etching with a KOH/H_2O_2 solution is an effective method for selectively removing metastable gallium-rich surface layer after FIB milling. Significantly, the etched surfaces are thermally stable and the surface roughness remains sub-nm even after post-annealing. The high thermal stability and sub-nm surface roughness improves the usability of FIB milled silicon for subsequent processes. As the wet etching of implanted silicon in KOH/H_2O_2 is self-terminated to a depth of ca. 30 nm for 30 keV ions, it can be used for defining nanoscale features for controlled nanofabrication by local implantation of gallium into silicon and subsequent removal of the gallium-rich surface.

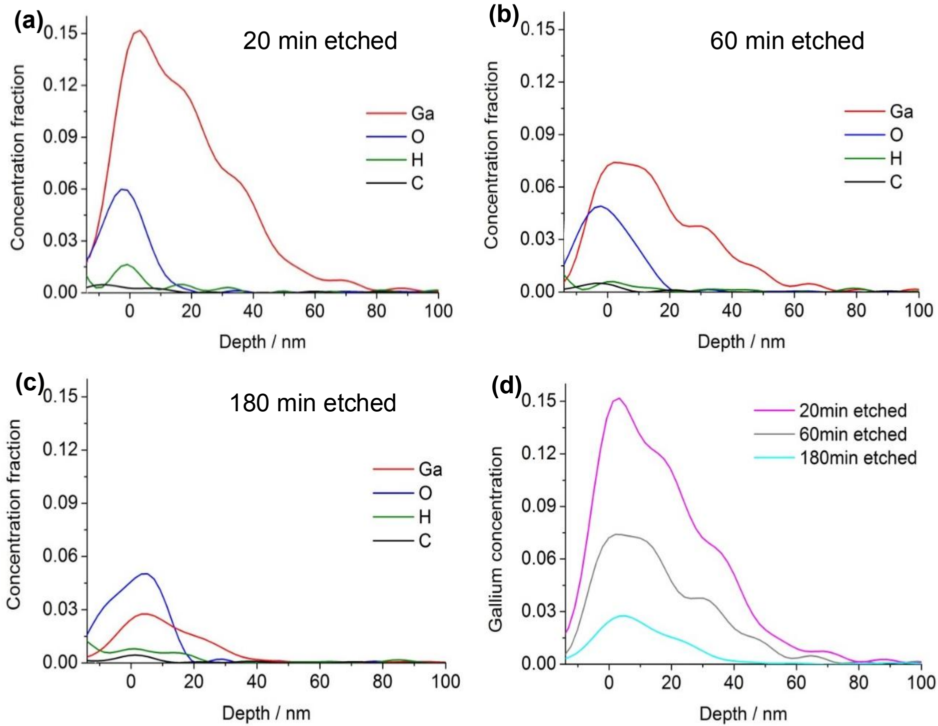

Figure 15 *Depth profiles of elements Ga, O, H, and C from ERDA measurements on a silicon substrate FIB milled and wet etched in the KOH/H_2O_2 solution for (a) 20, (b) 60 and (c) 180 minutes. (d) Comparision of Ga distribution for these three etching times. The milling ion dose was 8.34×10^{16} ions·cm^{-2} with a 30 keV ion beam.*

4.2 Thermal stability of FIB milled Al_2O_3 and Ta_2O_5 thin films

As seen in the post-annealing tests in Section 4.1, FIB milled silicon suffers from surface roughening upon heating during which gallium segregation occurs. One way to avoid the roughening is the use of hard mask layers that protect the silicon substrate from the FIB induced damage. Before making structures on the ALD grown Al_2O_3/Ta_2O_5/Al_2O_3 multilayers, the thermal stability of the FIB milled Al_2O_3 and Ta_2O_5 thin films was tested by post-annealing to see if segregation occurs on these two thin film materials [IV].

TMA and water were used as precursors to grow a single Al_2O_3 thin film on silicon at 250 °C in an ALD reactor while $Ta(OEt)_5$ and water were used for a single Ta_2O_5 thin film. Figures 16(a) and (b) show top-down views of FIB milled and post-annealed squares on 100 nm Al_2O_3 and 60 nm Ta_2O_5, respectively, on silicon substrates. A focused 30 keV, 100 pA gallium ion beam was used for milling 10 µm squares on the single thin films with various ion doses. The milled samples were then annealed at 250 °C in N_2 atmosphere for 10 min.

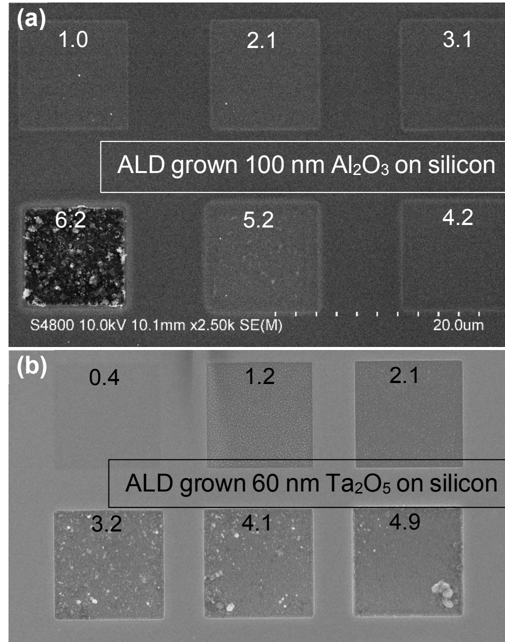

Figure 16 *SEM images of post-annealed surface with FIB milled squares on ALD grown thin films (a) 100 nm* Al_2O_3 *and (b) 60 nm* Ta_2O_5 *on silicon. A 30 keV gallium ion beam was used for milling and the value on each square is the ion dose (*$\times 10^{17}$ *ions·cm*$^{-2}$*). The samples were annealed at 250 °C in* N_2 *for 10 minutes after FIB milling.*

Gallium segregation appears only when the ion dose reaches 6.2×10^{17} ions·cm^{-2} for 100 nm Al_2O_3 and 3.2×10^{17} ions·cm^{-2} for 60 nm Ta_2O_5 as these doses have cut through the thin films and implanted gallium into bare silicon surface. The absence of the oxides on these two squares were verified by EDS measurements. The post-annealed squares, milled with ion doses lower than those needed to cut through the oxide thin films, are smooth and no segregation took place. In none of the samples, segregation was observed outside the milled squares (c.f. Figure 7). These observations demonstrate that the FIB milled Al_2O_3 and Ta_2O_5 thin films are thermally stable for subsequent processes where heating is needed such as PVD, ALD, or wet etching at elevated temperatures. The good thermal stability of these two thin film materials after FIB milling can be interpreted so that the implanted gallium ions are effectively trapped and stabilized into the oxides, which prevents the segregation.

Ion dose and energies determine the milled depths in the target materials. As explained above, the doses resulting in the rough squares after annealing in Figure 16 milled away the oxide layers. For 30 keV FIB, the ion dose 6.2×10^{17} ions·cm^{-2} is sufficient for milling away 100 nm Al_2O_3 film while 3.2×10^{17} ions·cm^{-2} are needed for 60 nm Ta_2O_5 film. These two ion doses will be used as reference values for milling of Al_2O_3 and Ta_2O_5 thin film stacks with 30 keV gallium ion beams.

4.3 Nanostructure fabrication

4.3.1 Nanopore arrays on silicon

The self-termination of the KOH/H_2O_2 etching of FIB milled silicon surface in Section 4.1.2 makes it interesting to see if the selective removal of the gallium-implanted silicon could be exploited for nanofabrication. Nanoscale gallium implantation was therefore done by low current beam as dot arrays and lines for subsequent wet etching[II].

Figure 17 schematically shows the fabrication steps for nanopore arrays on silicon. Local gallium implantation was first done by one-pass scanning of a 30 keV, 30 pA ion beam on silicon. The one-pass scanning was set to 5.0 ms spot exposures with 200 nm feature pitches, resulting in an implantation of a nanodot array. The following wet etching at room temperature locally removed the implanted volume and a nanopore array was formed.

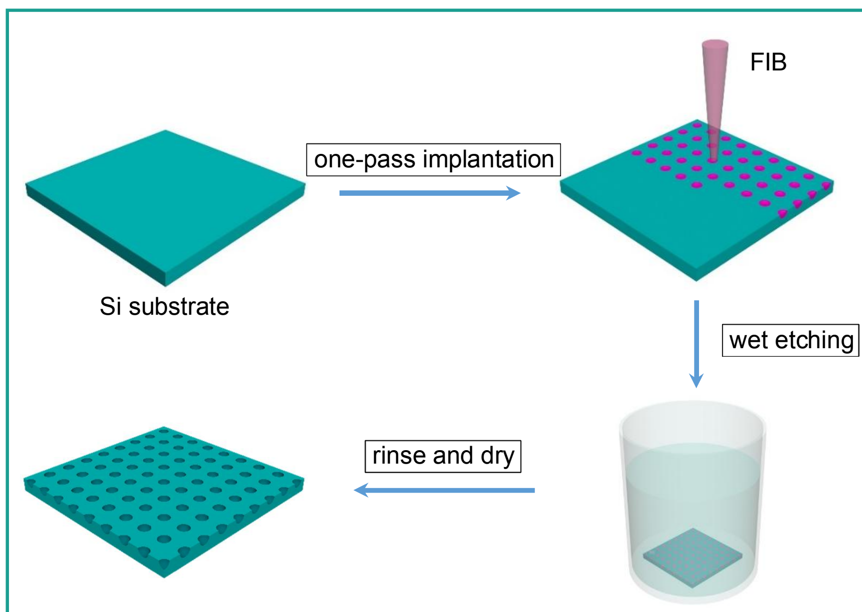

Figure 17 *Schematic illustration of fabrication steps for nanopore arrays. Gallium implantation into nanodot arrays is done by one-pass FIB milling and nanopore arrays are formed after wet etching in a* KOH/H_2O_2 *solution.*

Figures 18(a) and (b) are SEM images of an as-scanned nanodot array and wet etched surface, respectively. The deepening of the nanodots by the wet etching resulted in the formation of nanopores. AFM images shown in Figures 18(c) and (d) and the depth profile in Figure 18(e) are illustrations of the depth changes upon etching in the KOH/H_2O_2 solution. Before etching, only about 2.5 nm of material has been milled from the centers of the nanodots. Besides the slight milling of silicon, the implantation of gallium in silicon by the

one-pass scanning is visible in the contrast change of the nanodots with 100 nm diameter, shown in Figure 18(a). As seen in the SEM and AFM images of the post-etched surface, the material removal by wet etching is effectively limited into these nanodots. The opening of the nanopores remains the same as that of the nanodots but the depth at the feature center has increased by roughly 20 nm, being eight times that in the as-milled nanodots.

It should be noted that the shape of the pores formed is not as sharp as it may appear in Figure 18(e), as their depth (~22 nm) is much less than their opening (100 nm). Figure 18(f) presents a TEM cross-section view of the pores formed after the wet etching. The TEM sample was prepared along a pore row and the difference of the pore depths between the TEM and AFM results is due to the image plane being slightly off the center of the pores. An amorphized layer with a thickness of 40-50 nm was formed uniformly on the entire surface of the FIB scanned area, both inside and outside the implanted nanodots. This

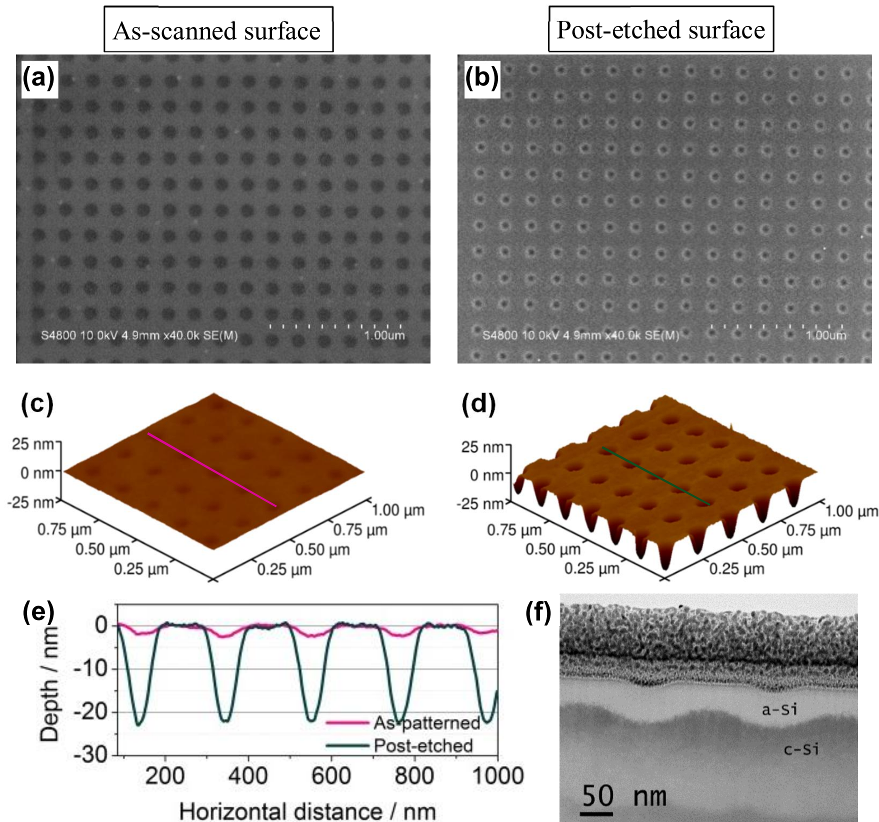

Figure 18 *(a) and (b) SEM images of single-pass milled and post-etched surfaces, respectively. (c) and (d) corresponding 3D images and (e) central profiles from AFM measurements. (f) TEM image of a nanopore array shown in Figures 18(b) and (d). The difference of the pore depths between the TEM and AFM results is due to the image plane in TEM being slightly off the pore centers.*

amorphized layer inside the nanopores agrees with the results from Section 4.1.2, such as gallium residue on the etched surface and the self-terminated etching of gallium implanted silicon in KOH/H_2O_2 solutions. The amorphization outside the nanopores is slightly less than inside and is caused by the overlapping beam tails from FIB implantation. The gallium ion beam does not have a staircase but a Gaussian profile, which means that some ions spread quite far from the beam center.

4.3.2 Nanotrenches on silicon

Besides nanodots, nanolines were also implanted into silicon by the low-current gallium ion beam, and the following wet etching of the gallium implanted silicon converted the nanolines to line trenches in the same way as in the fabrication of the nanopores[II]. Figure 19 is a TEM image of one trench, showing an amorphized silicon layer on the crystalline silicon. The amorphization extends hundreds of nanometers away from the line trench even though its thickness decreases with increasing distance from the trench.

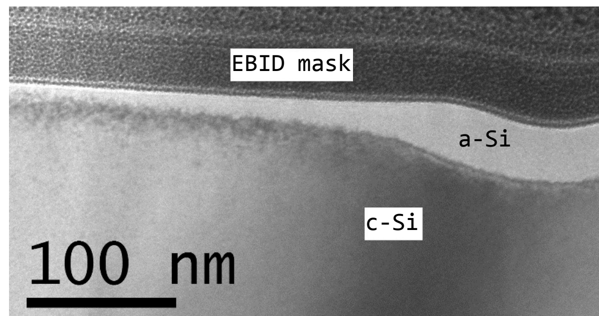

Figure 19 *TEM image of a line trench prepared by slight FIB milling and post-etching in KOH/H_2O_2.*

The gallium residues cause the amorphization and can not be entirely removed by the self-terminated wet etching. A protective mask layer may be applied on silicon before the FIB milling to minimize the implantation of gallium ions and thus prevent the amorphization. It is best to select a versatile material for the mask layer, for example, the material as such and after exposure to gallium ions must be easily removed during the etching step. Al_2O_3 grown by ALD was preferred because this amorphous thin film can be etched away in KOH/H_2O_2 and can be deposited at a low temperature with low carbon content and with precise thickness control.

Al_2O_3 thin films were grown on silicon wafers by ALD with TMA and H_2O as precursors. Lines were scanned by a 30 keV, 30 pA ion beam on the Al_2O_3 coated silicon to locally mill away the mask layer and implant gallium ions to the silicon. The ion dose was carefully tuned based on the milling rate from Section 4.2, so that the mask was removed from the line features but the milling of silicon was limited to a minimum. Figures 20(a) and (b) are TEM images of trenches formed with 30 nm and 50 nm mask layers, respectively. The Al_2O_3

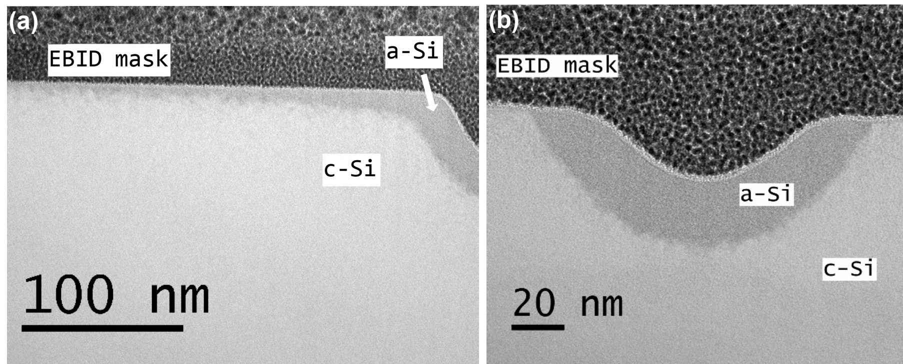

Figure 20 *TEM images of shallow line trenches fabricated by FIB patterning of a (a) 30 nm and (b) 50 nm Al_2O_3 mask layer on silicon and immediate wet etching in KOH/H_2O_2. The mask layer with 50 nm is thick enough to limit the ion-induced amorphization to the bottom and the sidewalls of the trench.*

mask layers were totally removed in KOH/H_2O_2 simultaneously with the self-terminated etching of the gallium-implanted silicon. Amorphization is still present on the surrounding surface with the 30 nm mask layer, but the amorphous layer is thinner than without a mask layer (Figure 19). With the 50 nm mask layer, the amorphization can be confined to only the bottom and sidewalls of the trench. The fabricated trench shown in Figure 20(b) is 90 nm wide and 24 nm deep, with an amorphized layer (20-30 nm thick) remaining after the self-terminated wet etching.

The ALD grown amorphous Al_2O_3 mask with a thickness of 50 nm worked well in this fabrication process. This FIB patterned mask layer was removed simultaneously with the self-terminated wet etching of the gallium implanted silicon surface. So silicon samples with a 50 nm thick Al_2O_3 mask can limit the tail effects of the ion beam and get thermally stabilized for further process at elevated temperatures. Amorphous Al_2O_3 thin films prepared with other deposition methods, such as PVD and CVD, could also work well as masks for FIB patterning.

To summarize the fabrication of nanopore arrays and line trenches, the self-termination of the room-temperature etching in KOH/H_2O_2 can be exploited in nanofabrication by local gallium implantation into silicon and subsequent selective removal of the gallium-rich part. After the etching, the gallium residue causes an amorphized layer with a smooth and thermally stable surface. The amorphized layer can be confined to the FIB milled silicon features by sacrificial mask layers, such as ALD grown Al_2O_3 films here, preventing amorphization of the surroundings of the milled features. The combination of local FIB patterning and selective gallium removal is thus a versatile approach for fabrication of nanoscale silicon structures.

4.3.3 Ta_2O_5 micro- and nanochannels

In this Section, micro- and nanochennels were prepared by combining FIB milling, wet etching and ALD of Ta_2O_5[III]. Silicon and silicon oxide have high selectivity in various etchants such as HF and KOH solutions. Thermal oxide can also be used as a mask for FIB patterning of opennings and KOH etching of silicon substrate through these openings. Figure 21 shows a schematic drawing of fabrication steps of nanochannels. FIB patterning and KOH etching make suspended SiO_2 structures on silicon. FIB patterned features including a circle, ring, square matrix and line set were demonstrated in paper III with more details. The wet etching contains three successive treatments in different etchants at room temperature: KOH/H_2O_2 (1 mol/L:1 mol/L) solution for removing the gallium-rich surface made by FIB patterning, 1 % HF for removal of the native oxide, and 1 mol/L KOH for anisotropic etching of silicon. The following ALD process coats the etched sample, making a three-dimensional coating over the structures created by wet etching. The thickness of the grown thin film increases along ALD cycles until the FIB openings are sealed and hollow channels are formed.

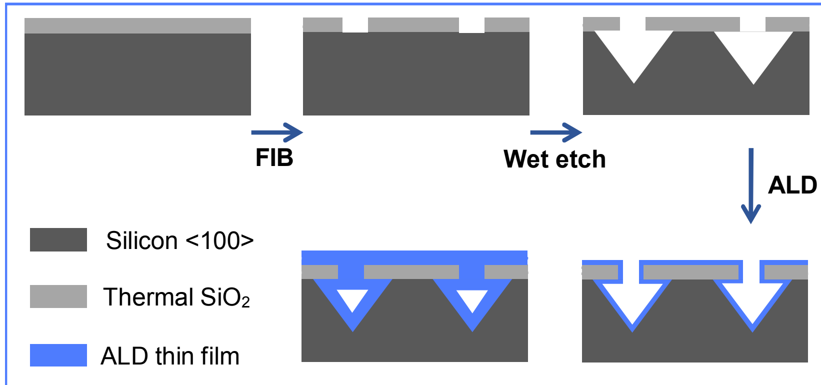

Figure 21 *Schematic illustration of fabrication steps for embedded nanochannels: FIB patterning to open lines on the top SiO_2, wet etching of Si, and ALD of a thin film for conformally coating the etch-formed trench until the self-sealing of FIB openings.*

Suspended SiO_2 structures were formed by anisotropically etching the underlying silicon through the FIB openings. The test of KOH etching of FIB implanted silicon surface, shown in Figure 11 (b), demonstrates that the gallium-implanted silicon serves as a mask for KOH etching of silicon. Therefore, the removal of gallium-rich surface is critical before KOH etching of silicon through the FIB-patterned openings where gallium implantation occurs.

The embedded channels are tunable by controlling their wall materials, thickness and the size of the trenches formed by wet etching. Ta_2O_5 thin films were grown with controlled thicknesses by ALD which is a versatile deposition method for coating three-dimensional templates. $Ta(OEt)_5$ and water were used as ALD precursors for growing Ta_2O_5 thin films at 250 °C. Ta_2O_5 was tested as the material of the channel walls because this amorphous, insulating and chemically stable oxide has various applications. A wide variety of wall

materials is available by using ALD to form micro- and nanochannels for specific applications. Channel walls consisting of multilayers of different materials can also be deposited by ALD before the FIB openings are sealed, and the thickness of each layer can be precisely controlled at a nanometer level by the number of ALD cycles.

The ion dose for opening the lines and the KOH etching time are significant process parameters for the size of the trenches. Note that the KOH etching of silicon does not proceed without removing most of the gallium with KOH/H_2O_2 (see Figure 11(b)). Figure 22(a) shows top-views of line sets patterned by FIB on SiO_2/silicon with increasing ion doses from left to right and etched with KOH for 0, 60, 80 and 120 min, respectively. The lateral etch distance increases with etching time, but is independent of ion dose. The suspended SiO_2 is stiff enough for self-supportance even in a much larger structure with a 10 μm SiO_2 plate (see paper III). Figure 22(b) shows cross-sectional SEM images of channels formed by ALD of a Ta_2O_5 thin film which eventually closed all the line openings. No channel was formed under the line A where the ion dose was so small that FIB made a V-shaped trench into only SiO_2 but did not reach the underlying silicon. This gallium-implanted SiO_2 layer prevents the wet etching of silicon. The ion dose for the line opening B was sufficient for the exposure of

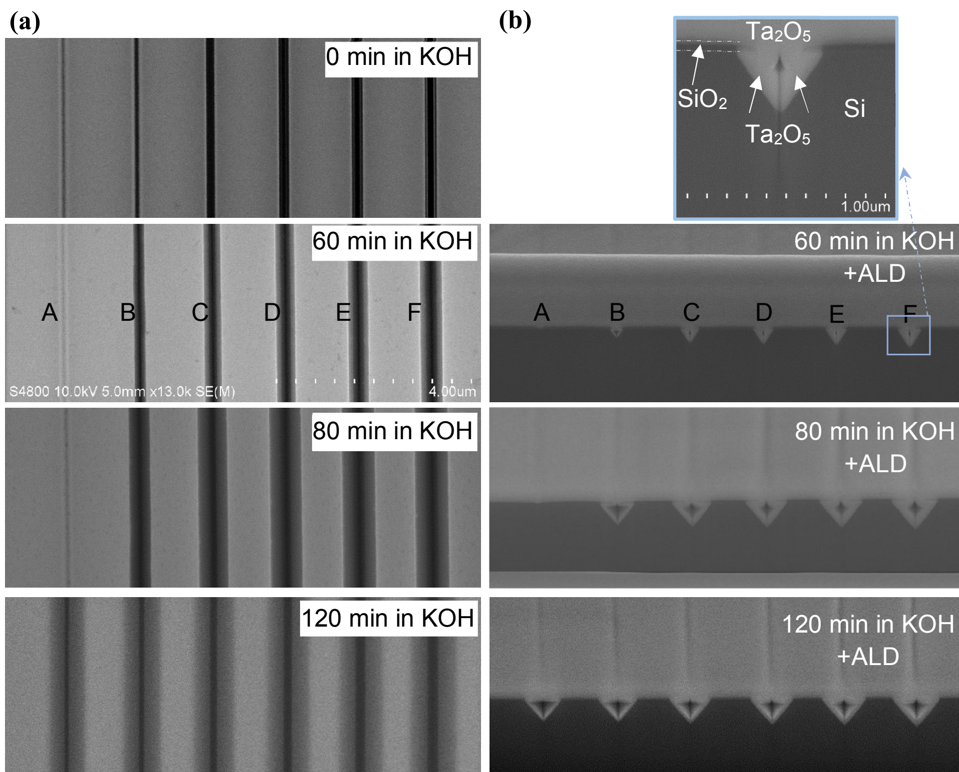

Figure 22 *(a) SEM images of FIB patterned and wet etched line openings with different etching durations in 1 mol/L KOH (b) Cross-sectional SEM images of the corresponding samples after ALD of* Ta_2O_5*. The distance of the adjacent milled line centers were all set to 1.5 μm.*

the underlying silicon which could therefore be anisotropically etched in the KOH solution. The ion dose increased from the line B to F, which resulted in wider line openings and led to deeper trenches after the KOH etching. The wider line openings in SiO_2 needed more ALD cycles for closing them. This resulted in thicker channel walls as the wall thickness of the channel equals to a half size of the line opening.

This resistless fabrication approach for Ta_2O_5 channels consists of FIB patterning, wet etching and ALD on thermally oxidized silicon surface where the wall thickness of the channels can be controlled by the ion dose and the channel size by the wet etching time. With the ALD coating of the 3D structures formed by the FIB patterning and wet etching, different wall materials can be selected, such as metals, oxides and nitrides, depending on the applications. The width and height of the resulting channels can be controlled down to sub-100 nm, making this approach highly versatile for nanochannel fabrication.

4.3.4 Ta_2O_5 nanowires

FIB patterning of multilayers consisting of oxides with different wet etch rates, such as Al_2O_3 and Ta_2O_5, is a potential way for preparing interesting self-supporting oxide nanostructures such as bridges and grid arrays. A nanowire fabrication procedure was demonstrated here based on the FIB milling and different etching rates of ALD grown Al_2O_3 and Ta_2O_5 thin films. An ALD grown $Al_2O_3/Ta_2O_5/Al_2O_3$ multilayer on silicon was FIB milled and chemically etched in 1 mol/L aqueous KOH. (Figure 23).

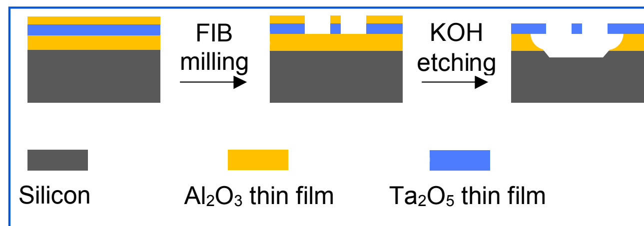

Figure 23 *Schematic illustration of fabrication steps for nanowires by FIB milling and KOH etching of an ALD grown multilayer ($Al_2O_3/Ta_2O_5/Al_2O_3$).*

A film stack was grown by ALD of sequential 100 nm Al_2O_3, 120 nm Ta_2O_5 and 50 nm Al_2O_3 thin films on silicon. Square patterns were milled and the spacing between the milled squares was varied. The top Al_2O_3 film (50 nm) served as a mask for FIB milling of the Ta_2O_5 film while the underlying Al_2O_3 spacer layer was etched from the sites opened by FIB. The spacer also trapped gallium ions from FIB and prevented them penetrating into the silicon. As a result of the high etching selectivity between the Al_2O_3 and Ta_2O_5 films, Ta_2O_5 bridges or nanowires were formed by controlling the etching time and the spacing between the milled squares. Figure 24 is a top-view of a Ta_2O_5 nanowire formed by FIB milling with a narrow gap between the squares and by wet etching in 1.0 mol/L KOH at room temperature for 100 min.

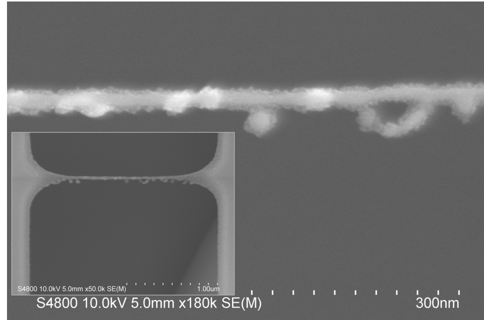

Figure 24 *SEM images of a Ta_2O_5 nanowire formed by wet etching after FIB patterning of an ALD grown film stack 100 nm Al_2O_3/120 nm Ta_2O_5/50 nm Al_2O_3.*

4.3.5 2D and 3D hard masks

As demonstrated in the previous section, ALD grown $Al_2O_3/Ta_2O_5/Al_2O_3$ multilayers can be used for nanostructure fabrication where the top Al_2O_3 is a mask for FIB patterning and the spacer Al_2O_3 leaves the Ta_2O_5 layer suspended after wet etching. The patterned and suspended Ta_2O_5 layer can be used as a mask for further processing, such as lift-off process. Different from the FIB patterning of larger areas to define nanowires in the previous section, here narrow features are FIB patterned to provide nano- and microscale openings in the Ta_2O_5 layer[IV]. A multilayer with sequentially deposited 200 nm Al_2O_3, 60 nm Ta_2O_5 and 50 nm Al_2O_3 was applied on a silicon (100) wafer which had been thermally oxidized to grow a layer of SiO_2 to protect silicon from the anisotropic etching in KOH. The Al_2O_3 mask layer is aimed to trap gallium ions outside the patterned area and to minimize widening of the FIB openings in the Ta_2O_5 layer. Besides trapping of gallium ions, the thicker Al_2O_3 spacer is used for wet etching and lift-off process. The thermal oxide protects silicon from wet etching, serving as an etch stop.

Figure 25(a) schematically illustrates the fabrication of 2D mask and metal structures on SiO_2 by FIB milling, TMAH etching, metal evaporation and lift-off . The ion dose for FIB milling was selected based on the values determined in Section 4.2 and verified by EDS measurements which showed that the Ta_2O_5 layer was certainly milled through. This allows the wet etching of the Al_2O_3 spacer and the formation of the 2D mask. The 2D mask enables fabrication of metal structures on SiO_2 by metal evaporation and lift-off. Figure 25(b) is a SEM image of the fabricated 2D mask with FIB milled 300 nm squares and 200 nm lines. ALD grown Al_2O_3 thin films are amorphous and etched isotropically in TMAH solutions. As clearly seen from the under-etch profile in Figure 25(b), the lateral etching rate of the Al_2O_3 spacer is about 38 nm/min in 5 % TMAH at 50 °C which is similar to the vertical etching rate determined in a separate test. The top Al_2O_3 layer has dissolved completely and the Ta_2O_5 mask became the top mask layer while the Al_2O_3 spacer was etched from the FIB opening sites down to the SiO_2 etch stop.

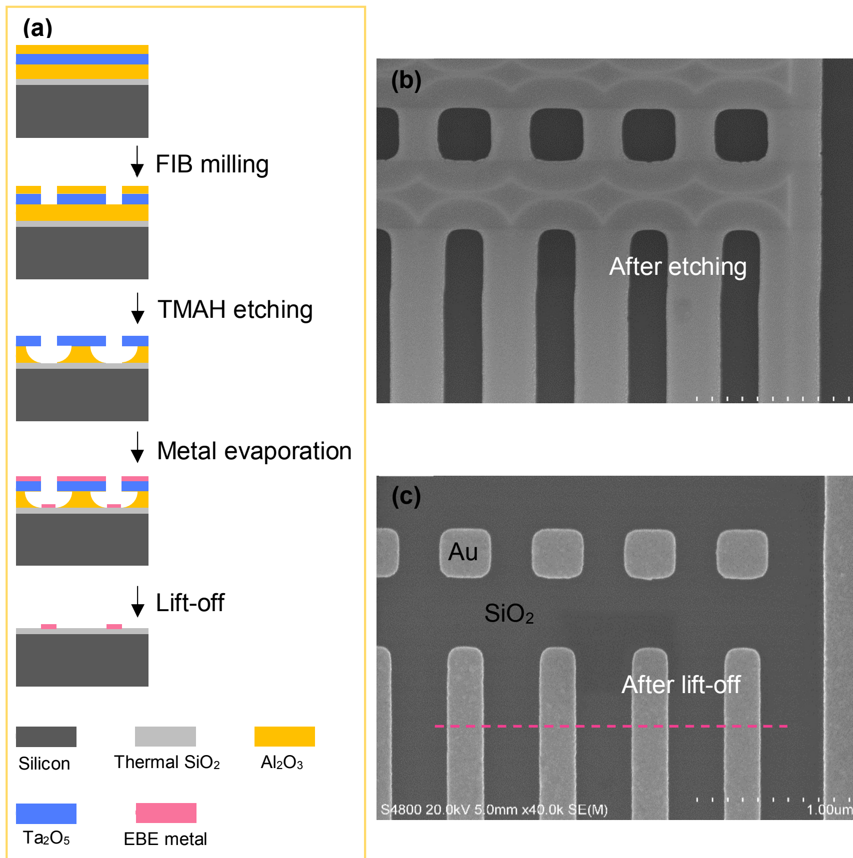

Figure 25 *(a) Schematic drawing of fabrication steps for 2D hard mask and metal pads on insulator: FIB milling of an $Al_2O_3/Ta_2O_5/Al_2O_3$ film stack, wet etching in TMAH, metal evaporation and lift-off. (b) SEM images of a 2D mask after FIB milling and TMAH etching, with 200 nm squares and 300 nm lines, and (c) metal pads fabricated by lift-off of the 2D mask after evaporation of Cr and Au.*

After the evaporation of Cr and Au on the fabricated 2D mask, lift-off was performed by further TMAH etching and ultrasonic rinsing in water. Figure 25(c) is an image of metal squares and lines formed after the lift-off process. The pattern was transferred from the FIB milled Ta_2O_5 mask to the metal structures retained on SiO_2 with smooth and sharp edges. Figure 26 is a cross-sectional TEM image of the fabricated metal lines where a lamella was cut and lifted-out along the dashline in Figure 25(b). The inset is a TEM image of a single metal line demonstrating that the metal layer is 50 nm thick, consisting of 12 nm Cr and 38 nm Au. The metal lines lay steadily on SiO_2 with a narrowing of the lines toward the top which is caused by the narrowing of the FIB openings during the evaporation of metals.

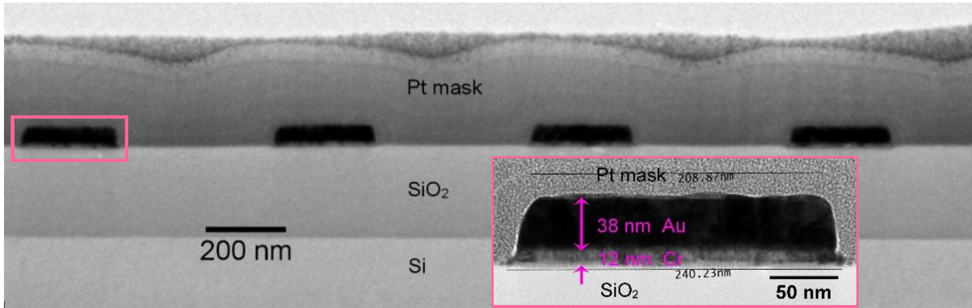

Figure 26 *TEM cross-sectional image of a lamella cut with FIB and lift out along the dash line in Figure 25(c). The inset is a detailed TEM image of the metal line inside the rectangle on the left side of the main image.*

In order to apply this approach for making 2D masks at a nanoscale level, smaller ion current (30 pA) was used for milling sub-100 nm features. The ALD grown $Al_2O_3/Ta_2O_5/Al_2O_3$ multilayer here includes 350 nm Al_2O_3 spacer, 60 nm Ta_2O_5 and 50 nm top Al_2O_3. Figure 27(a) is a SEM image of 16 lines scanned by FIB with decreasing ion doses from the left to right. The rectangles on both sides were milled for locating the nanolines. The sample was then wet etched in TMAH and aluminum metal was evaporated onto the 2D mask. Figure 27(b) is a TEM image of a lamella lifted-out along the dashline in Figure 27(a) after wet etching and aluminum evaporation. The Ta_2O_5 mask was suspended by under-etching from the line openings. The metal lines were formed by metal evaporation through the suspended mask and their widths were determined by the line opening widths. The ion doses for the lines O and P were not sufficient to open the lines through Ta_2O_5. The spacer Al_2O_3 under these two milled lines was blocked from being etched and thus no metal lines were formed. As higher ion doses made wider and deeper line openings, the wet etching completely removed the Al_2O_3 spacer under the openings A-G while increasing amount of Al_2O_3 remained under the openings J-N. There are also more and more Al_2O_3 residues under the mask bars between the adjacent line openings G-N. Aluminum lines stand steady on SiO_2 under the openings A-I, and on Al_2O_3 under the openings J-N with increasingly higher positions. The widths of the metal lines under the openings A-N decrease slightly because smaller ion doses made narrower line openings in the Ta_2O_5 mask. The line openings are narrowed and even closed during the metal evaporation, which causes narrower tops of the metal lines. The thickness of the metal line stopped increasing once the opening was closed before the end of the metal evaporation. The metal line in Figure 27(c) under the opening N is therefore the finest one with a width 60 nm and height 130 nm.

Nanoscale metal lines were fabricated with this 2D hard mask system. Milling the Ta_2O_5 mask with even smaller current or narrowing of the FIB milled line openings can be used for preparation of even finer features.

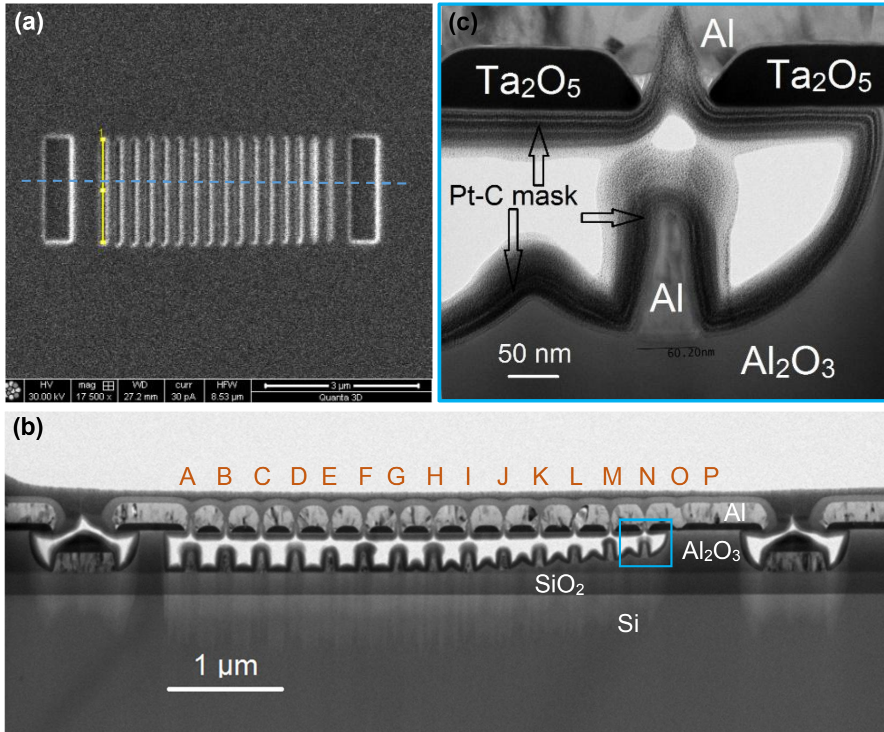

Figure 27 *(a) SEM image of FIB patterned narrow lines and two larger rectangles for navigating of the narrow lines (b) TEM image of a 2D mask and narrow metal lines fabricated by FIB patterning, wet etching and metal evaporation (c) enlarged TEM cross-sectional image of the narrowest metal line (site N).*

The cross-section image in Figure 27(b) also shows that the suspended Ta_2O_5 bars (2 µm length, ~200 nm width) between the adjacent line openings are stiff enough to hold the metal on top. However, the free ends of the mask bars in Figure 28 bent downward even though the bars were made from the same film stack with similar dimensions. This is the microstructure stiction phenomenon which is typically a problem in making freely suspended cantilevers and also a failure mode in MEMS devices[200]. The stiction of these mask bars causes a lift-off failure for the 2D masks here. On the other hand, the bending mask bars make a spatial connection between the mask layer and the SiO_2 layer with the spacer layer in between. This kind of interlayer connection has been exploited with sticking cantilevers by Takahashi et al[201] for electrical connections in MEMS devices.

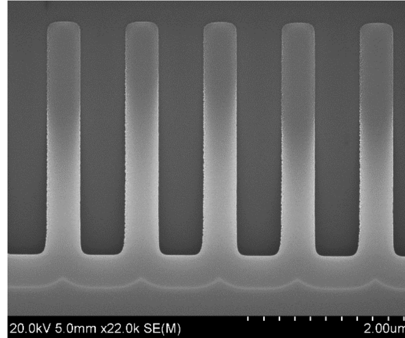

Figure 28 *SEM image of suspended Ta_2O_5 mask bars with the free ends sticking down.*

Another 2D mask was designed and made with FIB milling of two rings into the $Al_2O_3/Ta_2O_5/Al_2O_3$ stack and wet etching in the TMAH solution for 15 min. After evaporation of aluminum on this mask, two metal levels were formed: a bottom metal layer on SiO_2 and a top metal layer on Ta_2O_5, shown in Figure 29(a). These two metal levels are separated by a distinct vertical gap defined by the etched spacer. So the metal at the bottom of the ring trenches is isolated from the metals both on the circular mask pads and the surroundings. This isolation was verified by the lack of electrical connection when the two circular pads were contacted with probes. In the next sample, comb structures similar to that in Figure 28 were also prepared together with the two rings for intentional connection between the top and the bottom metal layers. Figure 29(b) shows a schematic drawing of the cross section of metal on a bent Ta_2O_5 bar making an interlayer connection and SEM images of the comb structures with metal on the suspended Ta_2O_5 bars bent to the SiO_2 surface. Electrical interlayer connection was realized by metal deposited on this interlayer-connected mask with intentionally made stiction.

With the interlayer metal connection by these comb structures, resistors can be made by FIB milling of one more trench in between the two ring trenches before the following etch step. As seen in Figure 29(c), the circular pads get electrically connected to the ring trenches which are connected by the trench in between. They all are isolated from the surroundings. The electrical resistance between the two pads was measured to be 90 Ω. The two pads can also be connected by various pathways. For example, the pathway shown in Figure 29(d) is 18 times longer than the direct line shown in Figure 29(c). The electrical resistance is 10 kΩ between the two pads in Figure 29(d).

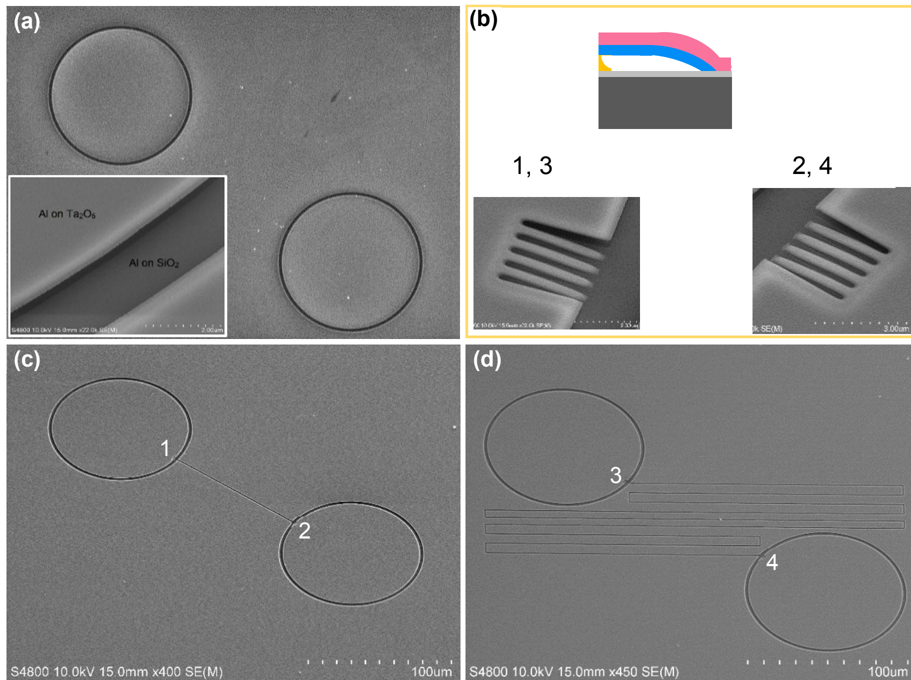

Figure 29 *(a) SEM image of FIB milled ring trenches on an $Al_2O_3/Ta_2O_5/Al_2O_3$ stack and the inset is a tilted image of a local isolation under the edge of the circular pads after wet etching and aluminum evaporation. (b) Schematic cross-section of interlayer metal connection and tilted SEM images of comb structures used for interlayer connection. (c) SEM image of a resistor with directly connected metal pads and (d) SEM image of a resistor where metal pads are connected with a longer pathway.*

As both FIB patterning and ALD are highly capable for 3D nanofabrication, also 3D masks were demonstrated with this film stack system. Thermally oxidized silicon sample was coated by evaporation of a gold thin film and then by ALD of an $Al_2O_3/Ta_2O_5/Al_2O_3$ stack. Micrometer sized gold balls are randomly splashed on the sample surface during the evaporation of gold thin films. 3D film stacks were conformally coated on the gold balls by ALD. 3D masks were fabricated by FIB milling and TMAH etching steps shown in Figure 30(a). Figures 30(b) and (c) are SEM images after FIB milling and wet etching, respectively. The 3D film stack was FIB milled through the Ta_2O_5 layer with one square at the top and four at the sides of the coated ball. After the TMAH etching, a hollow spherical shell was formed with the gold ball encaged inside. The outer diameter of this spherical structure is twice the thicknesses of Ta_2O_5 and spacer Al_2O_3 plus the diameter of the gold ball. The gap between the gold ball and Ta_2O_5 cage is in turn determined by the thickness of the Al_2O_3 spacer.

This demonstration of 3D hard mask fabrication takes the advantage of conformal coating of 3D substrates by ALD. The versatility of this patterning method for 2D and 3D masks has

great potential as the method combines the power of FIB patterning and the precise control of film thicknesses by ALD.

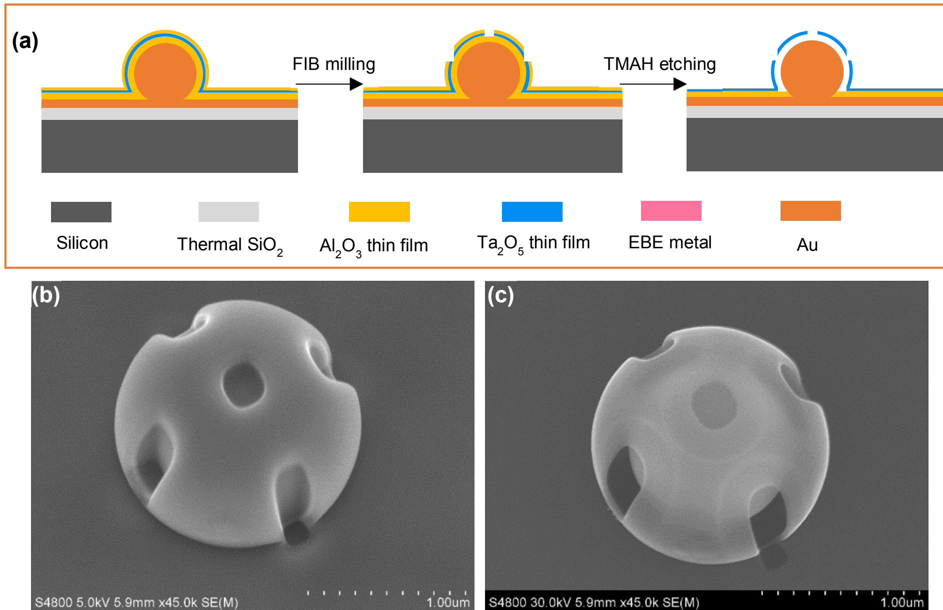

Figure 30 *(a) Schematic illustration of fabrication steps for 3D hard masks (b) SEM images of FIB milled 3D film stack ($Al_2O_3/Ta_2O_5/Al_2O_3$) on a gold particle and (c) SEM image of the fabricated 3D hollow structure.*

To conclude this nanofabrication section, hemispheric pores, line trenches, Ta_2O_5 nanochannels and nanowires, and 2D and 3D masks have been fabricated in this study by using FIB patterning, ALD of thin films and wet etching. The well organized arrays of hemispheric pores on silicon can be used, for example, as templates for making nanolens arrays[202]. The V-shaped line trenches can be applied as templates for metal filling without void formation or for ALD of different nanomaterials with even multilayers. The self-sealing nanochannels can be used for nanofluidics[203] or nanoscale vacuum transistors[204]. Self-suspended Ta_2O_5 nanowires can be applied for core-shell structure fabrication. The 2D masks have been demonstrated for fabrication of accurately defined metal nanowires, and thin film resistors with the realization of interlayer connections. The feasibility of combining ALD and FIB is verified by fabrication of these nanostructures and is also demonstrated for the 3D mask fabrication.

5 Conclusions

This thesis focuses on the feasibility of combining FIB and ALD that both already have high impact on 3D nanofabrication. The work started with the common issue: gallium implantation is an inherent event when focused gallium ion beams are used for milling of a substrate. This event becomes a severe problem when the implantation is undesired, especially for gallium implanted silicon surfaces which are metastable and lead to segregation of gallium upon mildest annealing.

Oblique incidence of the gallium ion beam was found an effective way to improve the thermal stability of gallium ion beam milled silicon surfaces. The implantation decreases with higher oblique incident angles and thus the surface gets more stable. A 50 nm thick Al_2O_3 thin film was proved to be a good mask for 30 keV FIB milling, which further stabilizes the gallium implanted silicon surface. We discovered one etchant, a KOH/H_2O_2 solution, which dissolves gallium-rich silicon layer at nanometre scales in a self-terminated manner. The dissolution also improves the thermal stability of gallium milled silicon and results in a sub-nm surface roughness. ALD grown Al_2O_3 and Ta_2O_5 thin films are both stable after FIB milling as the oxides effectively trap the implanted gallium ions.

ALD was found a feasible method to grow conformal thin films on FIB milled silicon surfaces even when segregation occurs. A 60° incident angle made the interface between the milled silicon and ALD grown Al_2O_3 smoother. Nanoscale V-shaped trenches were made by oblique FIB milling and ALD coating which is competent in narrowing gaps with good control of materials and dimensions. Nanopore arrays were fabricated by FIB implantation and removal of the gallium-rich silicon with KOH/H_2O_2. Materials other than silicon were tested for FIB milling, such as thermal SiO_2 and ALD grown Ta_2O_5 and $Al_2O_3/Ta_2O_5/Al_2O_3$ film stacks. Nanochannels and nanowires of Ta_2O_5, 2D masks for metal nanolines and 3D masks were fabricated by combining FIB, ALD and wet etching. Thin film resistors were also realized by the interlayer connection with controllable pathways made by FIB patterning.

These results demonstrate that it is feasible to combine FIB and ALD for nanofabrication when the FIB induced damage is minimized or the FIB patterned surfaces are thermally stable. This combination takes advantages of top-down processing from FIB and bottom-up processing from ALD, for controlling the dimensions and compositions of nanostructures.

References

1. R. P. Feynman, *Engineering and Science,* 1960, **23**, 22-36
2. N. Taniguchi, paper presented at the Proc. Intl. Conf. Prod. Eng., Tokyo, 1974.
3. G. Binnig, H. Rohrer, C. Gerber and E. Weibel, *Phys. Rev. Lett.,* 1982, **49**, 57-61
4. H. W. Kroto, J. R. Heath, S. C. O'brien, R. F. Curl and R. E. Smalley, *Nature,* 1985, **318**, 162-163
5. G. Binnig, C. F. Quate and C. Gerber, *Phys. Rev. Lett.,* 1986, **56**, 930-933
6. D. M. Eigler and E. K. Schweizer, *Nature,* 1990, **344**, 524-526
7. D. D. Majumder, R. Banerjee, C. Ulrichs, I. Mewis and A. Goswami, *IETE Technical Review,* 2007, **24**, 9-25
8. T. Ito and S. Okazaki, *Nature,* 2000, **406**, 1027-1031
9. B. Wu and A. Kumar, *Appl. Phys. Rev.,* 2014, **1**, 011104
10. C. J. Kang and S. C. Park, *CAP,* 2008, **8**, 656-658
11. B. D. Gates, Q. Xu, M. Stewart, D. Ryan, C. G. Willson and G. M. Whitesides, *Chem. Rev.,* 2005, **105**, 1171-1196
12. T. Weichelt, U. Vogler, L. Stuerzebecher, R. Voelkel and U. D. Zeitner, *Opt. Express,* 2014, **22**, 16310-16321
13. F. M. Schellenberg, *OptRv,* 2005, **12**, 83-89
14. S. Okazaki, *Microelectron. Eng.,* 2015, **133**, 23-35
15. Y. Xia, J. A. Rogers, K. E. Paul and G. M. Whitesides, *Chem. Rev.,* 1999, **99**, 1823-1848
16. Y. Chen, *Microelectron. Eng.,* 2015, **135**, 57-72
17. V. R. Manfrinato, L. Zhang, D. Su, H. Duan, R. G. Hobbs, E. A. Stach and K. K. Berggren, *Nano Lett.,* 2013, **13**, 1555-1558
18. V. R. Manfrinato, J. Wen, L. H. Zhang, Y. Yang, R. G. Hobbs, B. Baker, D. Su, D. Zakharov, N. J. Zaluzec, D. J. Miller, E. A. Stach and K. K. Berggren, *Nano Lett.,* 2014, **14**, 4406-4412
19. R. Garcia, A. W. Knoll and E. Riedo, *Nat. Nanotech.,* 2014, **9**, 577-587
20. A. A. Tseng, A. Notargiacomo and T. P. Chen, *J. Vac. Sci. Technol. B,* 2005, **23**, 877-894
21. D. Wouters and U. S. Schubert, *Angew. Chem. Int. Ed.,* 2004, **43**, 2480-2495
22. Y. S. Choi, X. Wu and D. W. Lee, *Rev. Sci. Instrum.,* 2014, **85**, 045002
23. R. D. Piner, J. Zhu, F. Xu, S. Hong and C. A. Mirkin, *Science,* 1999, **283**, 661-663
24. X. Wang and C. Liu, *Nano Lett.,* 2005, **5**, 1867-1872
25. S. Y. Chou, P. R. Krauss and P. J. Renstrom, *Science,* 1996, **272**, 85-87
26. Q. Xia and R. F. Pease, *Nanotechnology,* 2015, **26**, 182501
27. J. Qin, L. Ding and L. Wang, *Opt. Express,* 2015, **23**, 18518-18524
28. S. H. Ahn and L. J. Guo, *Adv. Mater.,* 2008, **20**, 2044-2049
29. C.-S. Kim, S.-H. Ahn and D.-Y. Jang, *Vacuum,* 2012, **86**, 1014-1035
30. A. A. Tseng, *Small,* 2005, **1**, 924-939
31. G. M. Whitesides and B. Grzybowski, *Science,* 2002, **295**, 2418-2421
32. C. Nicosia and J. Huskens, *Mater. Horiz.,* 2014, **1**, 32-45
33. A. K. Boal, F. Ilhan, J. E. DeRouchey, T. Thurn-Albrecht, T. P. Russell and V. M. Rotello, *Nature,* 2000, **404**, 746-748
34. C. Tang, E. M. Lennon, G. H. Fredrickson, E. J. Kramer and C. J. Hawker, *Science,* 2008, **322**, 429-432
35. K. W. Guarini, C. T. Black, Y. Zhang, I. V. Babich, E. M. Sikorski and L. M. Gignac, *2003 Ieee International Electron Devices Meeting, Technical Digest,* 2003, 541-544
36. D. J. Sellmyer, *Nature,* 2002, **420**, 374-375
37. D. E. Discher and R. D. Kamien, *Nature,* 2004, **430**, 519-520

38. R. Bogue, *Assembly Autom.,* 2008, **28**, 211-215
39. M. Ballauff, *Science,* 2016, **352**, 656-657
40. N. Bowden, A. Terfort, J. Carbeck and G. M. Whitesides, *Science,* 1997, **276**, 233-235
41. A. Terfort, N. Bowden and G. M. Whitesides, *Nature,* 1997, **386**, 162-164
42. D. H. Gracias, J. Tien, T. L. Breen, C. Hsu and G. M. Whitesides, *Science,* 2000, **289**, 1170-1172
43. V. E. Krohn, *J. Appl. Phys.,* 1962, **33**, 3523-3525
44. J. F. Mahoney, A. Y. Yahiku, H. L. Daley, R. D. Moore and J. Perel, *J. Appl. Phys.,* 1969, **40**, 5101-5106
45. V. E. Krohn and G. R. Ringo, *Appl. Phys. Lett.,* 1975, **27**, 479-481
46. R. L. Seliger, J. W. Ward, V. Wang and R. L. Kubena, *Appl. Phys. Lett.,* 1979, **34**, 310-312
47. R. G. Forbes, *Vacuum,* 1997, **48**, 85-97
48. H. P. Mayer, *Appl. Phys. Lett.,* 1985, **47**, 1247-1248
49. L. W. Swanson, G. A. Schwind and A. E. Bell, *J. Appl. Phys.,* 1980, **51**, 3453-3455
50. S. Hirohata, T. Kosugi, H. Sawaragi, R. Aihara and K. Gamo, *J. Vac. Sci. Technol. B,* 1992, **10**, 2814-2818
51. T. Radlička and B. Lencová, *Ultramicroscopy,* 2008, **108**, 445-454
52. P. Mazarov, A. Melnikov, R. Wernhardt and A. D. Wieck, *Appl. Surf. Sci.,* 2008, **254**, 7401-7404
53. L. W. Swanson, *Appl. Surf. Sci.,* 1994, **76**, 80-88
54. R. I. Hornsey, *Appl. Phys. A,* 1989, **49**, 293-297
55. L. Bischoff, *Nucl. Instrum. Methods Phys. Res. B,* 2008, **266**, 1846-1851
56. C. Akhmadaliev, L. Bischoff and B. Schmidt, *Mater. Sci. Eng., C,* 2006, **26**, 818-821
57. L. Bischoff, B. Schmidt, C. Akhmadaliev and A. Mücklich, *Microelectron. Eng.,* 2006, **83**, 800-803
58. F. Machalett and R. Mühle, *Rev. Sci. Instrum.,* 1996, **67**, 1015-1017
59. R. H. Higuchirusli and J. C. Corelli, *J. Appl. Phys.,* 1988, **63**, 603-610
60. A. Melnikov, M. Hillmann, I. Kamphausen, W. Oswald, P. Stauche, R. Wernhardt and A. D. Wieck, *Vacuum,* 2002, **67**, 249-251
61. A. Melnikov, T. Gerya, M. Hillmann, I. Kamphausen, W. Oswald, P. Stauche, R. Wernhardt and A. D. Wieck, *Nucl. Instrum. Methods Phys. Res. B,* 2002, **195**, 422-425
62. M. Itou, M. Kasai, T. Kimura, J. Yanagisawa, F. Wakaya, Y. Yuba and K. Gamo, *Nucl. Instrum. Methods Phys. Res. B,* 2003, **206**, 1013-1017
63. E. W. Müller, *Zeitschrift für Physik,* 1951, **131**, 136-142
64. E. W. Müller and K. Bahadur, *Phys. Rev.,* 1956, **102**, 624-631
65. E. W. Müller, *Science,* 1965, **149**, 591-&
66. E. W. Müller, *J. Appl. Phys.,* 1957, **28**, 1-6
67. W. H. Escovitz, T. R. Fox and R. Levisetti, *Proc. Natl. Acad. Sci. U.S.A.,* 1975, **72**, 1826-1828
68. N. P. Economou, J. A. Notte and W. B. Thompson, *Scanning,* 2012, **34**, 83-89
69. V. A. Zhukov and S. Kalbitzer, *Russian Microelectronics,* 2011, **40**, 17-24
70. V. N. Tondare, *J. Vac. Sci. Technol. A,* 2005, **23**, 1498-1508
71. Q. Ji, K. N. Leung, T. J. King, X. M. Jiang and B. R. Appleton, *Nucl. Instrum. Methods Phys. Res. B,* 2005, **241**, 335-340
72. P. Y. Nabhiraj, R. Menon, G. M. Rao, S. Mohan and R. K. Bhandari, *Nucl. Instrum. Methods Phys. Res. A,* 2010, **621**, 57-61
73. Y. S. Park, Y. Lee, Y. J. Kim, M. J. Park, D. W. Moon, K. J. Chung and Y. S. Hwang, *Rev. Sci. Instrum.,* 2012, **83**, 02B313
74. J. Orloff, *Rev. Sci. Instrum.,* 1993, **64**, 1105-1130
75. S. Kalbitzer, *Nucl. Instrum. Methods Phys. Res. B,* 1999, **158**, 53-60
76. Y. Lee, Q. Ji, K. N. Leung and N. Zahir, *Rev. Sci. Instrum.,* 2000, **71**, 722-724

77. R. Menon and P. Y. Nabhiraj, *Vacuum,* 2015, **111**, 166-169
78. S. K. Guharay, S. Douglass and J. Orloff, *Appl. Surf. Sci.,* 2004, **231**, 926-929
79. Y. Sakai, T. Yamada, T. Suzuki, T. Sato, H. Itoh and T. Ichinokawa, *Appl. Phys. Lett.,* 1998, **73**, 611-613
80. C. A. Volkert and A. M. Minor, *MRS Bull.,* 2007, **32**, 389-395
81. M. W. Phaneuf, *Micron,* 1999, **30**, 277-288
82. L. M. Keller, L. Holzer, R. Wepf, P. Gasser, B. Münch and P. Marschall, *Phys. Chem. Earth,* 2011, **36**, 1539-1544
83. M. Senoner and W. E. S. Unger, *J. Anal. At. Spectrom.,* 2012, **27**, 1050-1068
84. L. A. Giannuzzi and M. Utlaut, *Surf. Interface Anal.,* 2011, **43**, 475-478
85. L. D. Menard and J. M. Ramsey, *Nano Lett.,* 2011, **11**, 512-517
86. H. Lohmeyer, J. Kalden, K. Sebald, C. Kruse, D. Hommel and J. Gutowski, *Appl. Phys. Lett.,* 2008, **92**, 011116
87. Y. Chen, H. Chen, J. Yu, J. S. Williams and V. Craig, *Appl. Phys. Lett.,* 2007, **90**, 093126
88. C. Martelli, P. Olivero, J. Canning, N. Groothoff, B. Gibson and S. Huntington, *Opt. Lett.,* 2007, **32**, 1575-1577
89. D. J. Moss, V. G. Ta'eed, B. J. Eggleton, D. Freeman, S. Madden, M. Samoc, B. Luther-Davies, S. Janz and D. X. Xu, *Appl. Phys. Lett.,* 2004, **85**, 4860-4862
90. D. Petit, C. C. Faulkner, S. Johnstone, D. Wood and R. P. Cowburn, *Rev. Sci. Instrum.,* 2005, **76**, 026105
91. Y. Q. Chen, K. X. Bi, Q. J. Wang, M. J. Zheng, Q. Liu, Y. X. Han, J. B. Yang, S. L. Chang, G. H. Zhang and H. G. Duan, *ACS Nano,* 2016, **10**, 11228-11236
92. K. Jun and J. M. Jacobson, *Nano Lett.,* 2010, **10**, 2777-2782
93. D. Wang, Y. Q. Wang, X. D. Chen, Y. K. Zhu, K. Zhan, H. B. Cheng and X. Y. Wang, *Nanoscale,* 2016, **8**, 4107-4112
94. C. M. Lin, A. J. Steckl and T. P. Chow, *J. Vac. Sci. Technol. B,* 1988, **6**, 977-981
95. P. Chantrigarm, *2007 International Symposium on Integrated Circuits, Vols 1 and 2,* 2007, 146-149
96. N. E. Sosa, J. Liu, C. Chen, T. J. Marks and M. C. Hersam, *Adv. Mater.,* 2009, **21**, 721-725
97. S. A. Cybart, E. Y. Cho, T. J. Wong, B. H. Wehlin, M. K. Ma, C. Huynh and R. C. Dynes, *Nat. Nanotech.,* 2015, **10**, 598-602
98. X. Y. Wang, S. F. Xie, J. Liu, S. O. Kucheyev and Y. M. Wang, *Chem. Mater.,* 2013, **25**, 2819-2827
99. J. Han, T. G. Kim, B. K. Min and S. J. Lee, *Nanotechnology,* 2010, **21**, 485303
100. J. Han, T. G. Kim, B. K. Min and S. J. Lee, *Jpn. J. Appl. Phys.,* 2010, **49**, 06GK04
101. M. Erdmanis, P. Sievilä, A. Shah, N. Chekurov, V. Ovchinnikov and I. Tittonen, *Nanotechnology,* 2014, **25**, 335302
102. M. Erdmanis and I. Tittonen, *Appl. Phys. Lett.,* 2014, **104**, 073118
103. P. Peinado, S. Sangiao and J. M. De Teresa, *ACS Nano,* 2015, **9**, 6139-6146
104. Y. J. Ma, *Advances in Materials and Materials Processing, Pts 1-3,* 2013, **652-654**, 339-343
105. P. Dhakal, G. McMahon, S. Shepard, T. Kirkpatrick, J. I. Oh and M. J. Naughton, *Appl. Phys. Lett.,* 2010, **96**, 262511
106. R. Córdoba, M. Lorenzoni, J. Pablo-Navarro, C. Magén, F. Peréz-Murano and J. M. De Teresa, *Nanotechnology,* 2017, **28**, 445301
107. S. K. Tripathi and V. N. Kulkarni, *Nucl. Instrum. Methods Phys. Res. B,* 2009, **267**, 1381-1385
108. S. K. Tripathi, N. S. Rajput and N. Shukla, *Nucl. Instrum. Methods Phys. Res. B,* 2012, **288**, 6-9
109. L. E. Ocola, C. Rue and D. Maas, *MRS Bull.,* 2014, **39**, 336-341
110. L. A. Giannuzzi, J. L. Drown, S. R. Brown, R. B. Irwin and F. Stevie, *Microsc. Res. Tech.,* 1998, **41**, 285-290

111. M. Sugiyama and G. Sigesato, *J. Electron Microsc.,* 2004, **53**, 527-536
112. K. M. Krause, D. W. Vick, M. Malac and M. J. Brett, *Langmuir,* 2010, **26**, 17558-17567
113. H. H. Chen, V. H. Grassian, L. V. Saraf and A. Laskin, *Analyst,* 2013, **138**, 451-460
114. D. Vetterli, M. Döbeli, R. Mühle, P. W. Nebiker and C. R. Musil, *Microelectron. Eng.,* 1995, **27**, 339-342
115. Y. Sugimoto, M. Taneya, H. Hidaka and K. Akita, *J. Appl. Phys.,* 1990, **68**, 2392-2399
116. J. S. Yu, J. L. Liu, J. X. Zhang and J. S. Wu, *Mater. Lett.,* 2006, **60**, 206-209
117. G. Spoldi, S. Beuer, M. Rommel, V. Yanev, A. J. Bauer and H. Ryssel, *Microelectron. Eng.,* 2009, **86**, 548-551
118. T. L. Matteson, S. W. Schwarz, E. C. Houge, B. W. Kempshall and L. A. Giannuzzi, *J. Electron. Mater.,* 2002, **31**, 33-39
119. A. Lugstein, W. Brezna, G. Hobler and E. Bertagnolli, *J. Vac. Sci. Technol. A,* 2003, **21**, 1644-1648
120. L. Balcells, L. Abad, H. Rojas and B. Martínez, *Nanotechnology,* 2008, **19**, 135307
121. A. Persson, F. Riddar, H. Nguyen, F. Ericson and G. Thornell, *IEEE Trans. Magn.,* 2011, **47**, 151-155
122. B. Riedmüller, F. Huber and U. Herr, *J. Appl. Phys.,* 2014, **115**, 064307
123. R. W. Olesinski, N. Kanani and G. J. Abbaschian, *Bulletin of Alloy Phase Diagrams,* 1985, **6**, 362-364
124. A. Kannegulla and L. J. Cheng, *Nanotechnology,* 2016, **27**, 36LT01
125. Y. J. Xiao, F. Z. Fang, Z. W. Xu, W. Wu and X. C. Shen, *Nucl. Instrum. Methods Phys. Res. B,* 2013, **307**, 253-256
126. D. S. Ko, Y. M. Park, S. D. Kim and Y. W. Kim, *Ultramicroscopy,* 2007, **107**, 368-373
127. M. T. Langridge, D. C. Cox, R. P. Webb and V. Stolojan, *Micron,* 2014, **57**, 56-66
128. T. Suntola and J. Antson, *U.S. Patent,* 4,058,430, 1977
129. M. Leskelä and M. Ritala, *Angew. Chem. Int. Ed.,* 2003, **42**, 5548-5554
130. S. M. George, *Chem. Rev.,* 2010, **110**, 111-131
131. M. Ritala and M. Leskelä, *Nanotechnology,* 1999, **10**, 19-24
132. M. Leskelä, M. Kemell, K. Kukli, V. Pore, E. Santala, M. Ritala and J. Lu, *Mater. Sci. Eng., C,* 2007, **27**, 1504-1508
133. A. J. M. Mackus, A. A. Bol and W. M. M. Kessels, *Nanoscale,* 2014, **6**, 10941-10960
134. C. Marichy, N. Donato, M. Latino, M. G. Willinger, J. P. Tessonnier, G. Neri and N. Pinna, *Nanotechnology,* 2015, **26**, 024004
135. M. G. Willinger, G. Neri, E. Rauwel, A. Bonavita, G. Micali and N. Pinna, *Nano Lett.,* 2008, **8**, 4201-4204
136. K. Kukli, M. Ritala, M. Leskelä, T. Sajavaara and J. Keinonen, *J. Mater. Sci. - Mater. Electron.,* 2003, **14**, 361-367
137. M. Kemell, V. Pore, M. Ritala, M. Leskelä and M. Lindén, *J. Am. Chem. Soc.,* 2005, **127**, 14178-14179
138. M. Kemell, V. Pore, J. Tupala, M. Ritala and M. Leskelä, *Chem. Mater.,* 2007, **19**, 1816-1820
139. J. D. Caldwell, O. J. Glembocki, F. J. Bezares, M. I. Kariniemi, J. T. Niinistö, T. T. Hatanpää, R. W. Rendell, M. Ukaegbu, M. K. Ritala, S. M. Prokes, C. M. Hosten, M. A. Leskelä and R. Kasica, *Opt. Express,* 2011, **19**, 26056-26064
140. M. N. Liu, X. L. Li, S. K. Karuturi, A. I. Y. Tok and H. J. Fan, *Nanoscale,* 2012, **4**, 1522-1528
141. J. W. Li, X. Chen, W. H. Xu, C. Y. Nam and Y. Shi, *Thin Solid Films,* 2013, **536**, 275-279
142. S. H. Jin, G. H. Jun, S. H. Hong and S. Jeon, *Carbon,* 2012, **50**, 4483-4488
143. J. T. Korhonen, P. Hiekkataipale, J. Malm, M. Karppinen, O. Ikkala and R. H. A. Ras, *ACS Nano,* 2011, **5**, 1967-1974
144. R. J. Narayan, S. P. Adiga, M. J. Pellin, L. A. Curtiss, S. Stafslien, B. Chisholm, N. A. Monteiro-Riviere, R. L. Brigmon and J. W. Elam, *Mater. Today,* 2010, **13**, 60-64

145. M. Kariniemi, J. Niinistö, T. Hatanpää, M. Kemell, T. Sajavaara, M. Ritala and M. Leskelä, *Chem. Mater.,* 2011, **23**, 2901-2907
146. K. M. Price, K. E. Schauble, F. A. McGuire, D. B. Farmer and A. D. Franklin, *ACS Appl. Mater. Inter.,* 2017, **9**, 23072-23080
147. E. Färm, M. Kemell, M. Ritala and M. Leskelä, *J. Phys. Chem. C,* 2008, **112**, 15791-15795
148. C. Zhang, J. Kalliomäki, M. Leskelä and M. Ritala, *J. Vac. Sci. Technol. A,* 2018, **36**, 01B102
149. A. J. M. Mackus, S. A. F. Dielissen, J. J. L. Mulders and W. M. M. Kessels, *Nanoscale,* 2012, **4**, 4477-4480
150. J. Yoon, S. Kim and K. No, *Mater. Lett.,* 2012, **87**, 124-126
151. C. C. Wang, C. C. Kei, Y. W. Yu and T. P. Perng, *Nano Lett.,* 2007, **7**, 1566-1569
152. R. H. A. Ras, M. Kemell, J. de Wit, M. Ritala, G. ten Brinke, M. Leskelä and O. Ikkala, *Adv. Mater.,* 2007, **19**, 102-106
153. M. Mäkelä, T. Hatanpää, K. Mizohata, J. Räisänen, M. Ritala and M. Leskelä, *Chem. Mater.,* 2017, **29**, 6130-6136
154. M. Mäkelä, T. Hatanpää, K. Mizohata, K. Meinander, J. Niinistö, J. Räisänen, M. Ritala and M. Leskelä, *Chem. Mater.,* 2017, **29**, 2040-2045
155. M. Ritala, P. Kalsi, D. Riihelä, K. Kukli, M. Leskelä and J. Jokinen, *Chem. Mater.,* 1999, **11**, 1712-1718
156. M. Ritala, T. Asikainen, M. Leskelä, J. Jokinen, R. Lappalainen, M. Utriainen, L. Niinistö and E. Ristolainen, *Appl. Surf. Sci.,* 1997, **120**, 199-212
157. N. P. Dasgupta, X. B. Meng, J. W. Elam and A. B. F. Martinson, *Acc. Chem. Res.,* 2015, **48**, 341-348
158. V. Pore, M. Ritala and M. Leskelä, *Chem. Vap. Deposition,* 2007, **13**, 163-168
159. V. Miikkulainen, M. Leskelä, M. Ritala and R. L. Puurunen, *J. Appl. Phys.,* 2013, **113**, 021301
160. L. Niinistö, J. Päiväsaari, J. Niinistö, M. Putkonen and M. Nieminen, *Phys. Stat. Sol. A,* 2004, **201**, 1443-1452
161. M. Vehkamäki, T. Hatanpää, M. Kemell, M. Ritala and M. Leskelä, *Chem. Mater.,* 2006, **18**, 3883-3888
162. E. Härkönen, B. Díaz, J. Światowska, V. Maurice, A. Seyeux, M. Fenker, L. Tóth, G. Radnóczi, P. Marcus and M. Ritala, *Chem. Vap. Deposition,* 2013, **19**, 194-203
163. V. Pore, M. Dimri, H. Khanduri, R. Stern, J. Lu, L. Hultman, K. Kukli, M. Ritala and M. Leskelä, *Thin Solid Films,* 2011, **519**, 3318-3324
164. A. M. Schwartzberg and D. Olynick, *Adv. Mater.,* 2015, **27**, 5778-5784
165. M. Ritala, K. Kukli, A. Rahtu, P. I. Räisänen, M. Leskelä, T. Sajavaara and J. Keinonen, *Science,* 2000, **288**, 319-321
166. L. Tang, Q. C. Zhang, C. W. Li, X. N. Wang, K. Zhang, Y. C. Xu, T. T. Li, J. H. Fang and Y. G. Yao, *Carbon,* 2017, **114**, 224-229
167. J. X. Li, W. J. Liu, J. Y. Wang, I. Rozen, S. He, C. R. Chen, H. G. Kim, H. J. Lee, H. B. R. Lee, S. H. Kwon, T. L. Li, L. Q. Li, J. Wang and Y. F. Mei, *Adv. Funct. Mater.,* 2017, **27**, 1700598
168. J. K. Zhang, Z. B. Yu, Z. Gao, H. B. Ge, S. C. Zhao, C. Q. Chen, S. Chen, X. L. Tong, M. H. Wang, Z. F. Zheng and Y. Qin, *Angew. Chem. Int. Ed.,* 2017, **56**, 816-820
169. X. Liu, Q. Q. Zhu, Y. Lang, K. Cao, S. Q. Chu, B. Shan and R. Chen, *Angew. Chem. Int. Ed.,* 2017, **56**, 1648-1652
170. Q. Peng, X. Y. Sun, J. C. Spagnola, C. Saquing, S. A. Khan, R. J. Spontak and G. N. Parsons, *ACS Nano,* 2009, **3**, 546-554
171. S. Lee, A. R. Bielinski, E. Fahrenkrug, N. P. Dasgupta and S. Maldonado, *ACS Appl. Mater. Inter.,* 2016, **8**, 16178-16185
172. D. G. Wang, H. C. Chen, G. L. Chang, X. Lin, Y. Y. Zhang, A. Aldalbahi, C. Peng, J. Q. Wang and C. H. Fan, *ACS Appl. Mater. Inter.,* 2015, **7**, 14072-14078

173. J. Resasco, N. P. Dasgupta, J. R. Rosell, J. H. Guo and P. D. Yang, *J. Am. Chem. Soc.,* 2014, **136**, 10521-10526
174. B. Kalkofen, A. A. Amusan, M. S. K. Bukhari, B. Garke, M. Lisker, H. Gargouri and E. P. Burte, *J. Vac. Sci. Technol. A,* 2015, **33**, 031512
175. T. J. Park, P. Sivasubramani, B. E. Coss, H. C. Kim, B. Lee, R. M. Wallace, J. Kim, M. Rousseau, X. Y. Liu, H. Z. Li, J. S. Lehn, D. Hong and D. Shenai, *Appl. Phys. Lett.,* 2010, **97**, 092904
176. J. Malm, E. Sahramo, J. Perälä, T. Sajavaara and M. Karppinen, *Thin Solid Films,* 2011, **519**, 5319-5322
177. H. S. Moon, J. Y. Kim, H. M. Jin, W. J. Lee, H. J. Choi, J. H. Mun, Y. J. Choi, S. K. Cha, S. H. Kwon and S. O. Kim, *Adv. Funct. Mater.,* 2014, **24**, 4343-4348
178. S. Dhuey, C. Peroz, D. Olynick, G. Calafiore and S. Cabrini, *Nanotechnology,* 2013, **24**, 105303
179. S. Babin, G. Glushenko, T. Weber, T. Kaesebier, E. B. Kley and A. Szeghalmi, *J. Vac. Sci. Technol. B,* 2012, **30**, 031605
180. T. Weber, T. Käsebier, A. Szeghalmi, M. Knez, E. B. Kley and A. Tünnermann, *Nanoscale Res. Lett.,* 2011, **6**, 558
181. A. R. Bielinski, E. Kazyak, C. M. Schlepütz, H. J. Jung, K. N. Wood and N. P. Dasgupta, *Chem. Mater.,* 2015, **27**, 4799-4807
182. A. R. Bielinski, B. Boban, Y. He, E. Kazyak, D. H. Lee, C. M. Wang, A. Tuteja and N. P. Dasgupta, *ACS Nano,* 2017, **11**, 478-489
183. D. Dominguez, H. Borbn-Nuñez, J. Romo-Herrera, F. Muñoz-Muñoz, E. Reynoso-Soto, H. Tiznado and G. Soto, *J.Mater. Sci.,* 2018, **53**, 2005-2015
184. H. J. Shin, D. K. Jeong, J. G. Lee, M. M. Sung and J. Y. Kim, *Adv. Mater.,* 2004, **16**, 1197-1200
185. V. Miikkulainen, T. Rasilainen, E. Puukilainen, M. Suvanto and T. A. Pakkanen, *Langmuir,* 2008, **24**, 4473-4477
186. P. Chen, T. Mitsui, D. B. Farmer, J. Golovchenko, R. G. Gordon and D. Branton, *Nano Lett.,* 2004, **4**, 1333-1337
187. C. H. Lin, S. Polisetty, L. O'Brien, A. Baruth, M. A. Hilimyer, C. Leighton and W. L. Gladfelter, *ACS Nano,* 2015, **9**, 1379-1387
188. X. S. Chen, H. R. Park, M. Pelton, X. J. Piao, N. C. Lindquist, H. Im, Y. J. Kim, J. S. Ahn, K. J. Ahn, N. Park, D. S. Kim and S. H. Oh, *Nature Communications,* 2013, **4**, 2361
189. H. Im, K. C. Bantz, N. C. Lindquist, C. L. Haynes and S. H. Oh, *Nano Lett.,* 2010, **10**, 2231-2236
190. J. López, J. Martínez, N. Abundiz, D. Domínguez, E. Murillo, F. F. Castillón, R. Machorro, M. H. Farías and H. Tiznado, *Superlattices Microstruct.,* 2016, **90**, 265-273
191. A. Abou Chaaya, R. Viter, I. Baleviciute, M. Bechelany, A. Ramanavicius, Z. Gertnere, D. Erts, V. Smyntyna and P. Miele, *J. Phys. Chem. C,* 2014, **118**, 3811-3819
192. M. Mayer, K. Keskinbora, C. Grévent, A. Szeghalmi, M. Knez, M. Weigand, A. Snigirev, I. Snigireva and G. Schütz, *J. Synchrotron Rad.,* 2013, **20**, 433-440
193. K. Keskinbora, A. L. Robisch, M. Mayer, U. T. Sanli, C. Grévent, C. Wolter, M. Weigand, A. Szeghalmi, M. Knez, T. Salditt and G. Schütz, *Opt. Express,* 2014, **22**, 18440-18453
194. R. K. Ramachandran, J. Dendooven, M. Filez, V. V. Galvita, H. Poelman, E. Solano, M. M. Minjauw, K. Devloo-Casier, E. Fonda, D. Hermida-Merino, W. Bras, G. B. Marin and C. Detavernier, *ACS Nano,* 2016, **10**, 8770-8777
195. R. K. Ramachandran, M. Filez, J. Dendooven, V. V. Galvita, H. Poelman, E. Solano, E. Fonda, G. B. Marin and C. Detavernier, *RSC Adv.,* 2017, **7**, 20201-20205
196. J. Jokinen, J. Keinonen, P. Tikkanen, A. Kuronen, T. Ahlgren and K. Nordlund, *Nucl. Instrum. Methods Phys. Res. B,* 1996, **119**, 533-542
197. A. Mikkelsen, E. Hilner, J. N. Andersen, S. Ghatnekar-Nilsson, L. Montelius and A. A. Zakharov, *Nanotechnology,* 2009, **20**, 325304

198. L. Frey, C. Lehrer and H. Ryssel, *Appl. Phys. A,* 2003, **76**, 1017-1023
199. T. Radnai, S. Bálint, I. Bakó, T. Megyes, T. Grósz, A. Pallagi, G. Peintler, I. Pálinkó and P. Sipos, *Phys. Chem. Chem. Phys.,* 2014, **16**, 4023-4032
200. N. Tas, T. Sonnenberg, H. Jansen, R. Legtenberg and M. Elwenspoek, *J. Micromech. Microeng.,* 1996, **6**, 385-397
201. K. Takahashi, M. Mita, H. Fujita and H. Toshiyoshi, *IEICE Electron. Expr.,* 2006, **3**, 197-202
202. X. Y. Ling, C. Acikgoz, I. Y. Phang, M. A. Hempenius, D. N. Reinhoudt, G. J. Vancso and J. Huskens, *Nanoscale,* 2010, **2**, 1455-1460
203. S. W. Nam, M. H. Lee, S. H. Lee, D. J. Lee, S. M. Rossnagel and K. B. Kim, *Nano Lett.,* 2010, **10**, 3324-3329
204. J. W. Han, D. I. Moon and M. Meyyappan, *Nano Lett.,* 2017, **17**, 2146-2151